Versatile and High-Performance LiTaO$_2$:Tb^{3+}, Gd^{3+} Perovskite for Multimode Anti-counterfeiting, Flexible X-Ray Imaging, Continuous Stress Sensing, and Non-Real-Time Recording

Lyu, Tianshuai; Dorenbos, Pieter; Wei, Zhanhua

Important note
To cite this publication, please use the final published version (if applicable).
Please check the document version above.

Versatile and High-Performance LiTaO$_3$:Tb^{3+}, Gd^{3+} Perovskite for Multimode Anti-counterfeiting, Flexible X-Ray Imaging, Continuous Stress Sensing, and Non-Real-Time Recording

Tianshuai Lyu,* Pieter Dorenbos, and Zhanhua Wei

Multimode luminescence relates to how charge carriers are transported and recombined in response to various physical excitations. It shows promising applications in many fields like advanced anti-counterfeiting, information storage and encryption. Enabling a stable single compound with multimode luminescence is a unique technology but still remains a challenge. Herein, a versatile and high-performance energy storage LiTaO$_3$:0.01Tb^{3+},xGd^{3+} perovskite is discovered by utilizing the interplay of electron-trapping defect levels and hole-trapping Tb^{3+}. It combines an excellent charge carrier storage capacity ($\approx$7 and 12 times higher than state-of-the-art BaFBr(I):Eu^{2+} and Al$_2$O$_3$:C), >1200 h storage duration, >40 h afterglow, efficient optically stimulated luminescence, persistent mechanoluminescence, and force-induced charge carrier storage features. Particularly, it well responds to various stimuli channels, i.e., wide-range X-rays to 850 nm infrared photons, thermal activation, mechanical force grinding, or compression. To elucidate this multimode luminescence, charge carrier trapping and release processes in LiTaO$_3$:0.01Tb^{3+},xGd^{3+} with various physical stimulations will be unraveled by combining the vacuum-referred binding diagram construction, spectroscopy, thermoluminescence, and mechanoluminescence techniques. The versatile and high-performance LiTaO$_3$:0.01Tb^{3+},xGd^{3+} enables promising proof-of-concept multimode luminescence applications in advanced anti-counterfeiting, flexible X-ray imaging, continuous compression force sensing, and non-real-time recording.

T. Lyu, Z. Wei
Xiamen Key Laboratory of Optoelectronic Materials and Advanced Manufacturing
Institute of Luminescent Materials and Information Displays
College of Materials Science and Engineering
Huaqiao University
Xiamen 361021, China
E-mail: lv_tianshuai@126.com; lv_tianshuai@hqu.edu.cn
P. Dorenbos
Faculty of Applied Sciences, Department of Radiation Science and Technology
Delft University of Technology
Mekelweg 15, Delft 2629JB, The Netherlands

The ORCID identification number(s) for the author(s) of this article can be found under https://doi.org/10.1002/lpor.202300323

1. Introduction

Fake products like expensive medicines, foods, cigarettes, wines, electronics, and smart mobile phones appear in our daily life. The spread of fake products causes issues like global financial losses, human health damage, and security threat to both companies and society.[1] There are therefore demands for novel materials for advanced anti-counterfeiting technologies in various fields. During recent decades, the optical anti-counterfeiting technique receives a great deal of attention because the utilized luminescence materials exhibit many unique features like tailorable emission color, distinct lifetimes, and different emission routes upon different excitation.[2]

In general, different luminescence intensities, colors, and lifetimes can be used as unique features for conventional anti-counterfeiting applications.[3] Multimode luminescence is defined as the photon emission in response to multimode physical excitations for multimode applications. It receives growing attention because of its excellent coding capacity and confidentiality competencies.[4] It appears as a promising technique for advanced anti-counterfeiting applications.[5] In general, multimode luminescence can be obtained by admixing different materials with respective luminescence features, for example, CsPbBr$_3$ nanocrystal-based glass ceramics,[6] perovskite quantum dots,[7] organic compounds, transition or lanthanide ions doped inorganic phosphors,[8] metal halides,[9] or carbon dots.[10] Unfortunately, such mixture combinations often show low emission efficiency because of the physicochemical incompatibilities and the mismatches of properties. Enabling a stably single compound with multimode luminescence is a unique technology but still remains a challenge at present.

Generally, multimode luminescence is strongly associated with how free charge carriers (electrons and holes) are formed, transported, and recombined in a compound in response to various physical excitations, like optical, thermal, or mechanical stimulation.[11] To realize and regulate multimode luminescence,

ADVANCED
SCIENCE NEWS

www.advancedsciencenews.com

LASER
& PHOTONICS
REVIEWS

www.lpr-journal.org

the understanding of the trapping and de-trapping processes of charge carriers is crucial.[12] However, much research work is focused on the chemical synthesis of various compounds and their utilization in applications. The nature of charge carrier trapping and release processes in these synthesized compounds is often not deeply studied and remains unclear.[13] One reason is that defect energy level locations in compounds are often not known and systematic spectroscopy measurements are lacking.[14] Energy levels of defects are deduced by some chemists with computational methods. They can partly help to unravel luminescence mechanism but convincing clarification of the charge carrier trapping and release processes is still challenging. Therefore, there is scientific interest to develop a single compound with multimode luminescence by unraveling and controlling charge carrier trapping and de-trapping processes.

Mechanoluminescence materials are compounds that exhibit photon emissions upon mechanical stimulation. They have potential use in stress sensing-based applications,[15] like sensing solid contact, sensing airflow, and structural damage inspection of bridges and fans of wind-driven generators.[16] Mechanoluminescence can also be used as an important feature to establish multimode luminescence for advanced anti-counterfeiting.[17] Until now, ZnS:Cu+,Mn2+ is the best commercial mechanoluminescence compound. However, it is chemically unstable in humidity. There is ongoing research to develop alternatives.[18]

Charge carriers can be produced upon the stimulation of mechanical force. They can first be stored in traps and later liberated to yield photon emissions by thermal or optical stimulation. This strategy allows force non-real-time recording and readout,[19] which has promising use in multimode luminescence for anti-counterfeiting applications.

Charge carriers can be generated by X-ray exposure and then stored in traps in a storage phosphor for information storage applications. BaFBr(I):Eu2+ is a state-of-the-art X-ray storage phosphor until now. Similar to ZnS:Cu+,Mn2+, it is hygroscopic. New alternatives are also required to be developed. A flexible film detector can be prepared by dispersing storage phosphor powder in silicone gel. It then can be utilized for structural inspection by X-ray imaging of plane objects[11d]. **Figure 1**(a) compares the linear attenuation coefficients of LiTaO$_3$, BaFBr, and Al$_2$O$_3$ compounds. The ratios of the linear attenuation coefficients of LiTaO$_3$ perovskite at 20 and 150 keV to that of the BaFBr are $\approx$2.1 and 3.2. The density of LiTaO$_3$ ($\approx$7.45 g cm^{-3}) is significantly higher than that of BaFBr ($\approx$4.96 g cm^{-3}) and Al$_2$O$_3$ ($\approx$3.95 g cm^{-3}). It leads to enhanced photoelectric absorption in LiTaO$_3$ which is a requirement for developing promising storage phosphors.

Figure 1(b) provides the vacuum referred binding (VRBE) diagram of LiTaO$_3$ containing the energy level locations of Bi^{2+}, Bi^{3+}, different lanthanides, and defect levels that will be experimentally determined in LiTaO$_3$:Tb^{3+},xGd^{3+} in this work. In,[11c] Dy^{3+} was evidenced to act as a luminescence center to generate white persistent luminescence in LiTaO$_3$:Bi^{3+},Dy^{3+}. In,[11b,11c,12a] Bi^{3+} was evidenced to act as a shallow ($\approx$0.6 eV) electron trap in LiTaO$_3$ which is not deep enough for thermally stable electron storage at room temperature (RT). Very intense initial afterglow appears in Bi^{3+} co-codoped LiTaO$_3$ at RT. It leads to rapid loss of stored charge carriers which is then not suitable for long-term information storage applications. In, Ref. [20] Eu^{3+} was evidenced to act as a $\approx$0.8 eV deep electron trap in LiTaO$_3$. However, the Eu^{3+}

co-doped LiTaO$_3$:Ln^{3+},Eu^{3+} (Ln = Tb or Pr) still suffered from moderate fading of stored charged carriers at RT. Particularly, the charge carriers stored at Eu^{2+} cannot be excited by mechanical stimulation to produce Ln^{3+} emission. LiTaO$_3$:Ln^{3+},Eu^{3+} then cannot be used for smart stress sensing applications. The VRBE diagram in Figure 1(b) has not yet been used to exploit the development of storage phosphor in lanthanides-only doped LiTaO$_3$.

In this work, a versatile and high-performance LiTaO$_3$: 0.01Tb^{3+},xGd^{3+} energy storage perovskite was discovered by using the interplay of electron trapping defect levels and hole trapping Tb^{3+} in Figure 1(b). LiTaO$_3$:0.01Tb^{3+},xGd^{3+} combines an excellent charge carrier storage capacity ($\approx$7 and 12 times higher than commercial BaFBr(I):Eu^{2+} and Al$_2$O$_3$:C), >1200 h storage duration, >40 h afterglow, X-ray excited emission, optically stimulated luminescence, persistent mechanoluminescence, and force-induced charge carrier storage features. Particularly, it well responds to various stimuli channels, i.e., wide-range X-rays to 850 nm infrared photons, thermal activation, mechanical force grinding, or compression. These features enable promising applications like multimode anti-counterfeiting, flexible X-ray imaging, continuous compression force sensing, and non-real-time recording as illustrated in Figure 1(c).

2. Results

2.1. Spectroscopy Properties, Charge Carrier Trapping, and De-Trapping Processes by Thermal or Optical Stimulation in LiTaO$_3$:Tb^{3+},xGd^{3+}

Figure 2(a) gives the XRD patterns of the LiTaO$_3$:0.01Tb^{3+},xGd^{3+} ($x = 0 - 0.015$) compounds. The collected XRD patterns match well with that of the standard LiTaO$_3$ (PDF#29-0836) pattern. This implies that the Gd^{3+} co-doping does not lead to impurity phases and single-phase LiTaO$_3$:0.01Tb^{3+},xGd^{3+} compounds were obtained.

To unravel how the Gd^{3+} dopant is distributed in LiTaO$_3$: 0.01Tb^{3+},xGd^{3+}, Figure 2(b1–b6) shows the high-resolution transmission electron microscope photographs for the typical LiTaO$_3$:0.01 Tb^{3+},0.005Gd^{3+}. The elements of tantalum, oxygen, terbium, and gadolinium are uniformly distributed through the crystals.

To study the optical properties of LiTaO$_3$:0.01Tb^{3+},xGd^{3+}, their photoluminescence emission and excitation spectra at RT are first provided in Figure 2(c,d). Characteristic Tb^{3+} $^5D_4\rightarrow^7F_j$ ($j = 0$–6) emissions appear upon 285 nm excitation. The excitation spectrum ($\lambda_{em} = 544$ nm) is constituted of an excitation band peaked at $\approx$252 nm and a broad shoulder band peaked at $\approx$285 nm. The host excitation is at 224 nm as was concluded[12a] from the PLE spectrum ($\lambda_{em} = 452$ nm) of LiTaO$_3$ host at 10 K shown in Figure 2(d). The excitation band peaked at 252 nm appears at just lower energy and is observed in the undoped LiTaO$_3$ host and in LiTaO$_3$ doped with Tb^{3+}, Pr^{3+}, Eu^{3+}, or Gd^{3+}. The 252 nm band is then attributed to either an unknown host intrinsic defect(s) or to near Tb^{3+}, Pr^{3+}, Eu^{3+}, or Gd^{3+} exciton creation. The shoulder band is attributed to intervalence charge transfer (IVCT) from Tb^{3+} to the LiTaO$_3$ conduction band (CB), i.e., Tb$^{3+}\rightarrow$CB IVCT.[21] With increasing x in LiTaO$_3$:0.01Tb^{3+},xGd^{3+}, the Tb$^{3+}\rightarrow$CB IVCT band gradually decreases with respect to the 252 nm band.
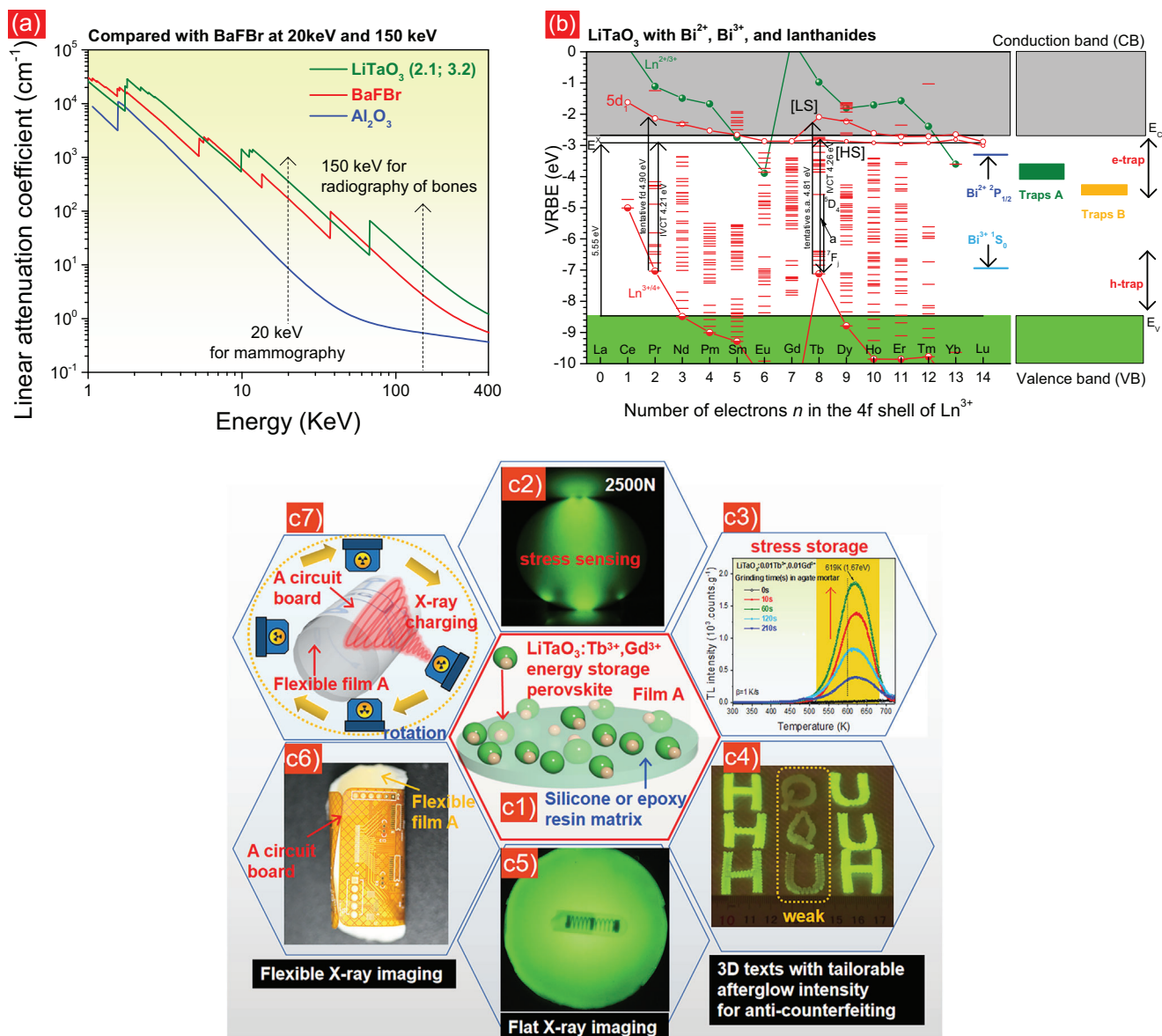
Figure 1. a) Comparison of linear attenuation coefficients of $LiTaO_3$, Al_2O_3, and BaFBr. b) Vacuum-referred binding energy diagram for the discovered $LiTaO_3$:Tb^{3+},Gd^{3+}. c1–c7) Illustration on how the developed $LiTaO_3$:Tb^{3+},Gd^{3+} storage phosphor can be used for multimode applications in flexible X-ray imaging, multimode anti-counterfeiting, continuous stress sensing, and non-real-time recording.

To further unravel the luminescence property of $LiTaO_3$:$0.01Tb^{3+}$,xGd^{3+}, the PLE and PL spectra of a typical $LiTaO_3$:$0.01Tb^{3+}$,$0.005Gd^{3+}$ in the spectral range from 125 to 700 nm at 10 K were measured and shown in Figure 2(e). The excitation spectrum contains a shoulder band peaked at $\approx$196 nm and two strong excitation bands peaked at $\approx$241.5 and $\approx$283 nm. Bands narrow at lower temperatures and the 252 nm band at RT shifts to shorter wavelengths at 10 K. Both bands are better resolved in Figure 2(e). The 241.5 nm band at 10 K is the same as the 252 nm band at RT. The 283 nm band at 10 K is the same as the 285 nm band at RT. Similar to Figure 2(d), the two excitation bands are assigned to the unintended defect(s) and the $Tb^{3+}{\rightarrow}CB$ IVCT in Figure 2(e). Upon 196 nm excitation, the $LiTaO_3$:$0.001Tb^{3+}$,$0.005Gd^{3+}$ compound is excited across the

bandgap with the following energy transfer to Tb^{3+}. Tb^{3+} might also be excited to one of its 5d states at 196 nm excitation. Typical Tb^{3+} $^5D_4{\rightarrow}^7F_j$ (j = 0–6) line emissions emerge upon 285 nm excitation, which is similar to that in Figure 2(c). Gd^{3+} emission was not observed around 310 nm.

Figure 2(f) shows the X-ray excited emission spectra of the $LiTaO_3$:$0.01Tb^{3+}$,$0.005Gd^{3+}$ and a BaF_2 reference sample recorded at 120 s after the X-ray tube is switched on. BaF_2 gives a broad emission band with a maximum of $\approx$ 315 nm because of self-trapped-exciton recombination luminescence.[22] Its absolute scintillation light yield is 10 000 photons per MeV of absorbed amount of ionizing radiation (ph MeV^{-1}).[23] Upon X-ray excitation, characteristic Tb^{3+} $^5D_4{\rightarrow}^7F_j$ emissions are observed which are similar to that upon UV 285 nm excitation
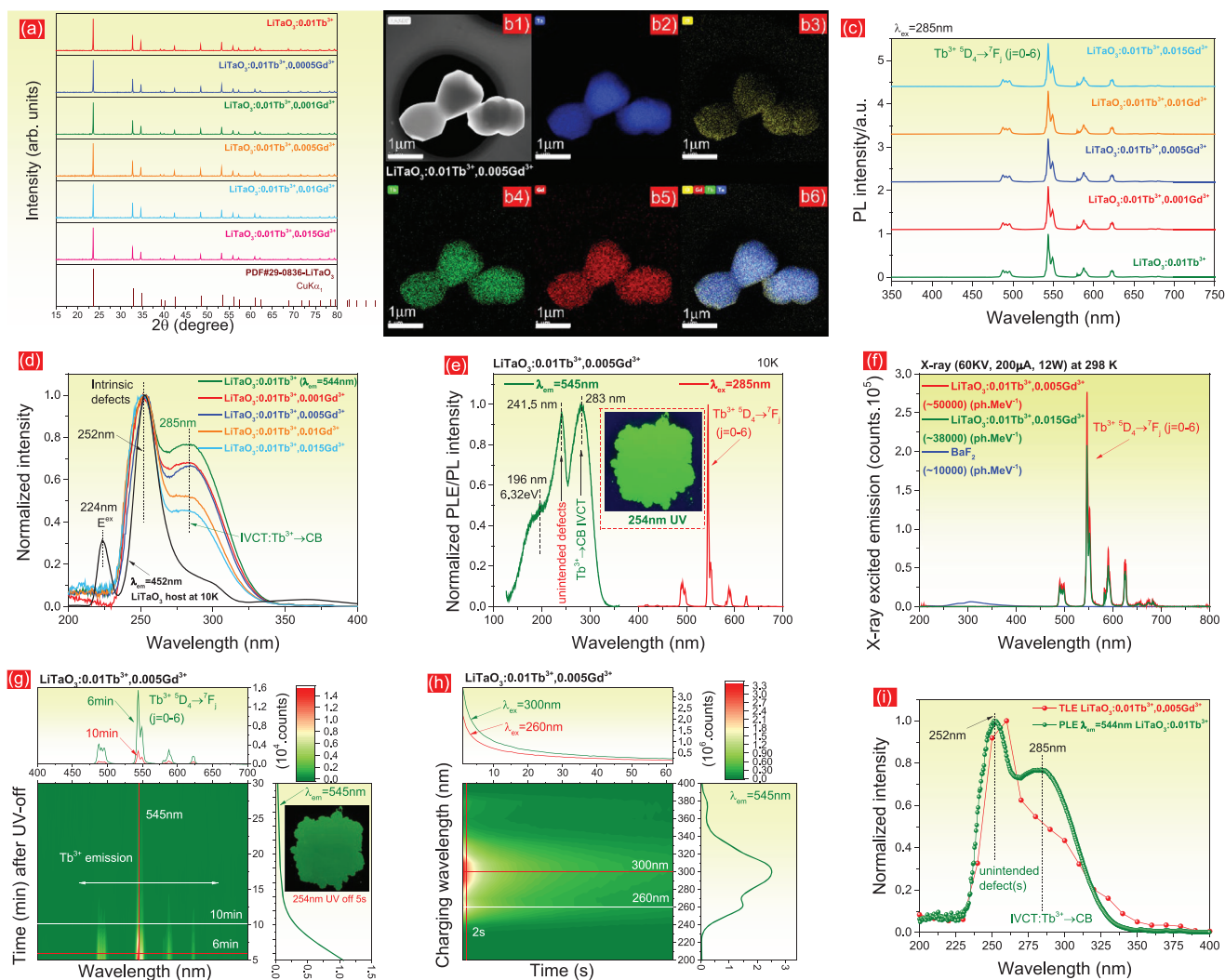
Figure 2. a) XRD patterns, b) transmission electron microscope images, c–e) photoluminescence excitation and emission spectra, f) X-ray excited emission spectra, g) a 2D contour plot of RT isothermal decay spectra after 254 nm UV-light charging, h) a 2D contour plot of RT isothermal decay curves after different energy photon charging, and i) a comparison of thermoluminescence excitation (TLE) curve and photoluminescence excitation spectrum (PLE) for the LiTaO$_3$:0.01Tb^{3+},xGd^{3+}.

in Figure 2(c,e). Compared with the X-ray excited emission spectrum of BaF$_2$, the absolute scintillation light yield for LiTaO$_3$:0.01Tb^{3+},0.005Gd^{3+} was determined to be ≈50 000 ph MeV$^-$. It is ≈6 or ≈1.3 times higher compared with the state-of-the-art scintillators Bi$_4$Ge$_3$O$_{12}$ (8.2×10^3 ph MeV^{-1}) or NaI:Tl (3.8×10^4 ph MeV^{-1})[24a]. Note that the decay time of LiTaO$_3$:0.01Tb^{3+},0.005Gd^{3+} (≈0.7 ms)[24] is longer than that of Bi$_4$Ge$_3$O$_{12}$ (≈0.3 μs) and NaI:Tl (≈0.23 μs)[24a].

To study the charge carrier trapping and de-trapping processes in LiTaO$_3$:0.01Tb^{3+},0.005Gd^{3+}, RT isothermal afterglow spectra as a function of time after 254 nm UV-light charging was first recorded and provided in Figure 2(g). Typical Tb^{3+} $^5D_4 \rightarrow ^7F_j$ (j = 0–6) emissions are visible in the dark, which can be observed more than 0.5 h in the dark.

Figure 2(h) shows a 2D contour plot for RT isothermal afterglow curves of LiTaO$_3$:0.01Tb^{3+}, 0.005Gd^{3+} irradiated by different energy photons from 200 to 400 nm for 60 s. Figure 2(i)

compares the thermoluminescence excitation (TLE) curve of LiTaO$_3$:0.01Tb^{3+},0.005Gd^{3+} with the photoluminescence excitation (PLE) spectrum of LiTaO$_3$:0.01Tb^{3+} (λ_{em} = 544 nm). The LiTaO$_3$:0.01Tb^{3+},0.005Gd^{3+} storage phosphor can be charged via the optical excitation at the excitation band peaked at ≈252 nm and the Tb$^{3+} \rightarrow$CB IVCT band peaked at ≈285 nm.

To further unravel the charge carrier trapping and release processes, LiTaO$_3$:0.01Tb^{3+},xGd^{3+} compounds were investigated in detail. **Figure 3**(a) first gives the X-ray excited integrated emission intensities from 300 to 750 nm as a function of time for LiTaO$_3$:0.01Tb^{3+},xGd^{3+}. LiTaO$_3$:0.01Tb^{3+}, 0.0005Gd^{3+} has the strongest emission intensity (curve 2), while LiTaO$_3$:0.01Tb^{3+},0.015Gd^{3+} has the weakest emission intensity (curve 6). With increasing time, all emission curves gradually increase. It means that some traps are gradually filled with time and more free charge carriers are available to yield the Tb^{3+} $^5D_4 \rightarrow ^7F_j$ emissions.
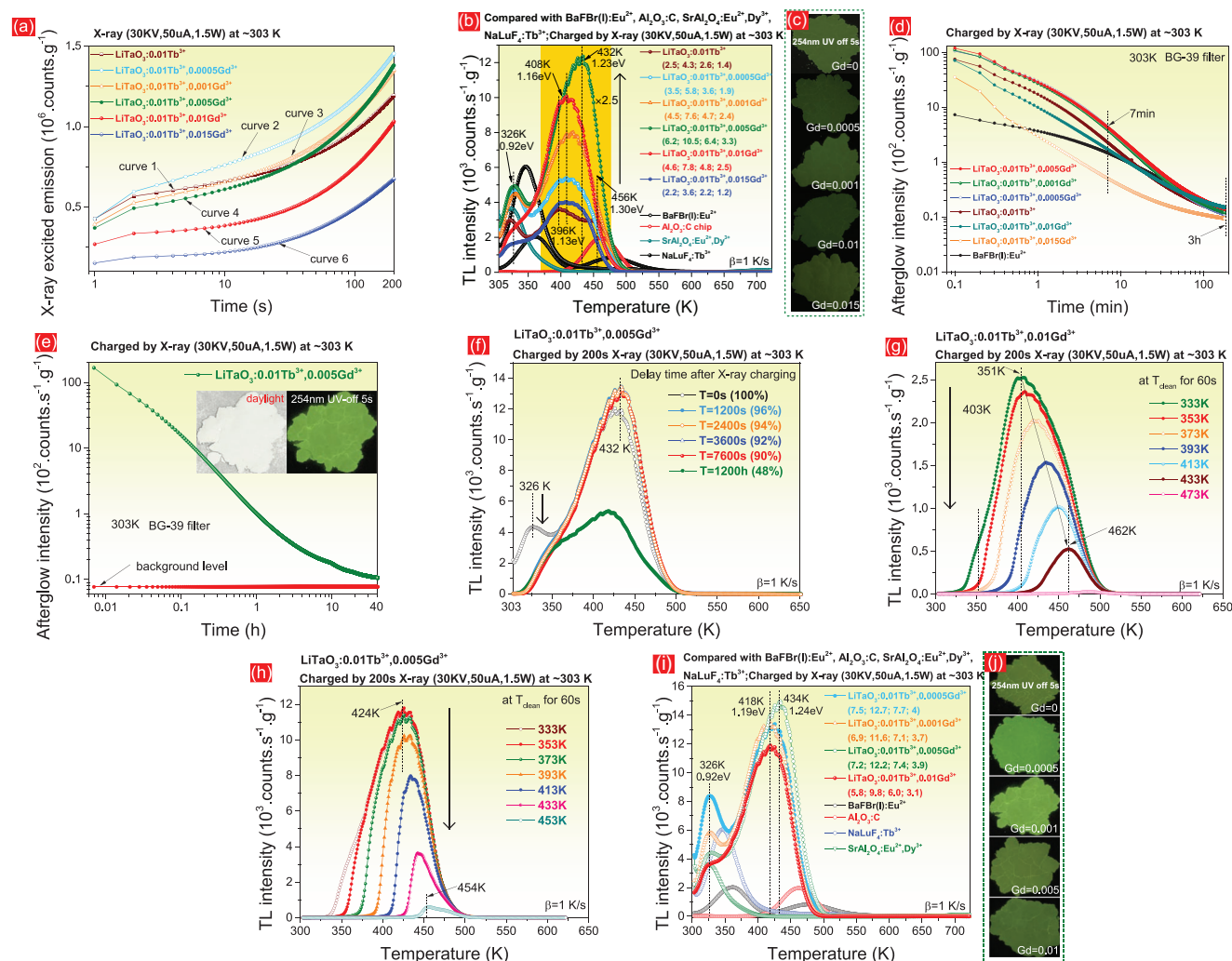
Figure 3. a) X-ray excited emission intensities as a function of time, b) TL glow curves at $\beta = 1$ K s^{-1} after X-ray charging, c) afterglow photographs recorded at 5s after 254 nm UV-light charging, d) 3 h, e) 40 h RT isothermal decay curves, and f) TL fading characteristics with different delay time after X-ray charging for LiTaO$_3$:0.01Tb^{3+},xGd^{3+} (x = 0 − 0.015). TL glow curves after different peak cleaning at T$_{clean}$ for g) LiTaO$_3$:0.01Tb^{3+},0.01Gd^{3+} and h) LiTaO$_3$:0.01Tb^{3+},0.005Gd^{3+}. i) TL glow curves at $\beta = 1$ K s^{-1} after X-ray charging and j) afterglow photographs measured at 5 s after 254 nm UV-light charging for the optimized LiTaO$_3$:0.01Tb^{3+},xGd^{3+}. The emission from 300 to 750 nm was monitored.

Figure 3(b) shows the TL glow curves at $\beta = 1$ K s^{-1} for LiTaO$_3$:0.01Tb^{3+},xGd^{3+} charged by X-rays. For LiTaO$_3$:0.01Tb^{3+}, TL glow bands peaked at ≈322, ≈396, and ≈456 K appear. For LiTaO$_3$:0.01Tb^{3+},xGd^{3+}, there is a TL band peaked near 326 K and a broad TL glow band in the temperature range from 350 to 525 K. Since these TL glow bands appear in all samples, they will be attributed to unintended defects in LiTaO$_3$:0.01Tb^{3+},xGd^{3+}. The trapping depths were roughly estimated and given in the legend of Figure 3(b) by utilizing the following first-order TL-recombination kinetics formula[12b,26]:

$$\ln\left(\frac{T_m^{\,2}}{\beta}\right) = \frac{E}{kT_m} + \ln\left(\frac{E}{ks}\right) \tag{1}$$

in which T_m is the experimentally observed peak maximum of a TL glow band, β denotes the utilized heating rate ($\beta = 1$ K s^{-1}), E is the trap depth, k is the Boltzmann constant (8.62×10^{-5} eV

K^{-1}), and s denotes the frequency factor of $s = 2 \times 10^{13}$ s^{-1} which is estimated from the maximum phonon frequency in LiTaO$_3$ (660 cm^{-1}).[26]

The optimized NaLuF$_4$:Tb^{3+}(15 mol%)@NaYF$_4$ persistent luminescence nanocrystals were utilized for comparison study. The NaLuF$_4$:Tb^{3+}(15 mol%)@NaYF$_4$ reference sample was synthesized by the authors.[27] Herein, it is abbreviated as NaLuF$_4$:Tb^{3+}. The ratios named as (n1; n2; n3; n4) of the integrated TL intensities from 305 to 700 K for LiTaO$_3$:0.01Tb^{3+},xGd^{3+} (x = 0 − 0.015) to that of the state-of-the-art (n1) BaFBr(I):Eu^{2+}, (n2) Al$_2$O$_3$:C disc, (n3) SrAl$_2$O$_4$:Eu^{2+},Dy^{3+}, or (n4) NaLuF$_4$:Tb^{3+} are provided in the legend of Figure 3(b). Compared with Tb^{3+} single-doped LiTaO$_3$:0.01Tb^{3+}, Gd^{3+} co-doping leads to much stronger TL intensities in LiTaO$_3$:0.01Tb^{3+},xGd^{3+} (x = 0.0005 − 0.01). Particularly, ≈ 2.5 times stronger TL intensity and very high ratios of (6.2; 10.5; 6.4; 3.3) were observed in LiTaO$_3$:0.01Tb^{3+},0.005Gd^{3+}.

ADVANCED
SCIENCE NEWS

www.advancedsciencenews.com

LASER
& PHOTONICS
REVIEWS

www.lpr-journal.org

Since the TL glow band peaked near 326 K in Figure 3(b) is close to RT, de-trapping of stored charge carriers is expected to occur at RT. Figure 3(c) demonstrates that RT afterglow photographs of LiTaO$_3$:0.01 Tb^{3+},xGd^{3+} indeed emerge in the dark after 254 nm UV-light charging. The RT isothermal decay curves of LiTaO$_3$:0.01Tb^{3+},xGd^{3+} in Figure 3(d) further demonstrate that >3 h persistent luminescence can be observed after X-ray charging for 10 min. Particularly, the RT isothermal decay curve in Figure 3(e) shows that more than 40 h Tb^{3+} $^5D_4\rightarrow^7F_j$ afterglow can be observed after X-ray charging for 0.5 h.

Figure 3(f) shows the TL glow curves of LiTaO$_3$:0.01Tb^{3+}, 0.005Gd^{3+} charged first by 200 s X-rays and then followed by different delay times from 0s to 1200 h prior to TL-readout. The ratios of the integrated TL intensity from 303 to 650 K with no delay to that with different delay times are provided as percentages in the legend of Figure 3(f). The TL intensity remains 90% for t = 7600s and 48% for t = 1200 h.

Since LiTaO$_3$:0.01Tb^{3+},0.005Gd^{3+} and LiTaO$_3$:0.01Tb^{3+}, 0.01Gd^{3+} have excellent charge carrier storage ability, the nature of traps was studied further. The compound was first irradiated by X-rays for 200s at $\approx$303 K and then kept at a fixed temperature named T_{clean} for a duration of one minute. The compound was then cooled to RT and subsequently a TL glow curve was collected at a heating rate (β) of 1 K s^{-1}. Figure 3(g,h) shows the TL glow curves with different T_{clean} for LiTaO$_3$:0.01Tb^{3+},0.01Gd^{3+} and LiTaO$_3$:0.01Tb^{3+},0.005Gd^{3+}. With increasing T_{clean}, the TL intensity gradually decreases and the TL glow peak shifts toward a higher temperature. This means that a wide trap depth distribution exists in LiTaO$_3$:0.01Tb^{3+},xGd^{3+}. The electrons stored at less deep traps have been liberated at T_{clean} and only the part of electrons stored at deep traps still remained. The trap depth distribution is estimated in the range from 1.00 eV to 1.32 eV by utilizing Equation (1) with the frequency factor of $s = 2 \times 10^{13}$ s^{-1}, β = 1 K s^{-1}, and the TL glow peak maximum (T_{max}) ranging from 351 K to 462 K in Figure 3(g).

To obtain better charge carrier storage capacity, LiTaO$_3$: 0.01Tb^{3+},xGd^{3+} was optimized by synthesizing at 1250 °C. Figure 3(i) compares the TL glow curves of the optimized LiTaO$_3$:0.01Tb^{3+},xGd^{3+} (x = 0 − 0.01) measured at β = 1 K s^{-1} after X-ray charging for 200s. Two TL glow bands peaked near 326 K and $\approx$418-434 K with stronger TL intensities appear. Particularly, as shown in the legend of Figure 3(i), very high ratios of (7.2; 12.2; 7.4; 3.9) appear in the optimized LiTaO$_3$:0.01Tb^{3+},0.005Gd^{3+}. Figure 3(j) shows that, compared with x = 0.0005 and 0.001, LiTaO$_3$:0.01Tb^{3+},0.005Gd^{3+} and LiTaO$_3$:0.01Tb^{3+}, 0.01Gd^{3+} have less initial afterglow intensities. It means that they are potential good storage phosphors for applications.

Figure 4(a) gives the TL glow curves at β = 1 K s^{-1} for LiTaO$_3$: 0.01Tb^{3+},0.01Gd^{3+} irradiated by X-rays with different duration from 30 − 600 s. The integrated TL intensities from 303 to 700 K as a function of X-ray exposure time are provided in the inset in Figure 4(a). They can be well fitted by a linear equation of TL = 316 613 × t−4.71 × 10^6 (R^2 = 0.999). The similar applied to LiTaO$_3$:0.01Tb^{3+},0.005Gd^{3+} as shown in Figure S11 (Supporting Information). It implies that they can be utilized as potential dosimeters for X-ray detection.

To study how the stored charge carriers are liberated by optical stimulation, Figure 4(b) gives the TL glow curves of LiTaO$_3$:0.01Tb^{3+},0.01Gd^{3+} first irradiated by 254 nm UV-light for 20s and then exposed to different energy photon stimulation with a duration of 10s. The ratios of integrated TL intensity irradiated only by 254 nm UV-light to that of with additional photon stimulation are given as percentages in the legend of Figure 4(b). Figure 4(c) further shows the TL glow curves of LiTaO$_3$:0.01Tb^{3+},0.01Gd^{3+} first exposed to 20s 254 nm UV-light and then subjected to WLED illumination with different duration from 1−120 s. Upon 1 s or 120 s WLED stimulation, $\approx$34% or $\approx$92% trapped charge carriers were efficiently released via an optically stimulated luminescence route. The TL curves in Figure 4(d) further demonstrate that 120 s 850 nm infrared light stimulation can liberate $\approx$30% trapped charge carriers during exposure to 300 s X-rays

Figure 4(e1) gives the RT isothermal decay curve of LiTaO$_3$: 0.01Tb^{3+},0.01Gd^{3+} first exposed to 300 s X-rays and then illuminated by infrared 850 nm light. Compared with that with no 850 nm infrared light stimulation in Figure 4(e2), $\approx$ 24 times stronger Tb^{3+} $^5D_4\rightarrow^7F_j$ emissions emerge in Figure 4(e1) when the 850 nm infrared light is turned on. This is because the trapped electrons are released by the 850 nm stimulation to recombine with holes trapped at Tb^{4+}, yielding characteristic Tb^{3+} $^5D_4\rightarrow^7F_j$ (j = 0–6) emissions.

Figure 4(b,d) demonstrates that the TL glow band peaked at 323 K and can be significantly decreased by optical stimulation. It implies that much weaker Tb^{3+} $^5D_4\rightarrow^7F_j$ persistent luminescence can be observed in the phosphor area with optical stimulation. This feature has been utilized to rapidly exhibit two afterglow texts of "S" and "r" in the LiTaO$_3$:0.01Tb^{3+},0.01Gd^{3+} based film as shown in Figure 4(f4,f5), where a commercial 656 nm laser beam was utilized in Figure 4(f3). The similar applied to LiTaO$_3$:0.01Tb^{3+},0.005Gd^{3+} in Figure S12 (Supporting Information).

Figure 4(f6) shows an afterglow photograph of LiTaO$_3$: 0.01Tb^{3+},0.01Gd^{3+} based phosphor film which is first exposed to 254 nm UV-light and then illuminated by 905 nm infrared laser array from an iPhone 12Pro. The intense Tb^{3+} green emission array is visible to the naked eye in the dark. It indicates in Figure 4(f1–f6) that the 905 or 656 nm infrared light stimulated Tb^{3+} emissions in LiTaO$_3$:0.01Tb^{3+},0.01Gd^{3+} are efficient and flexible to design afterglow logos for exploring anti-counterfeiting application.

2.2. Mechanically Induced Charge Carrier Storage for Non-Real-Time Force Recording Application

To determine whether charge carriers can be stored via mechanical stimulation, LiTaO$_3$:0.01Tb^{3+}, xGd^{3+} storage phosphors were ground in an agate mortar. **Figure 5**(a,b) gives the TL glow curves of LiTaO$_3$:0.01Tb^{3+},0.0005Gd^{3+} and LiTaO$_3$:0.01Tb^{3+},0.01Gd^{3+} ground with different duration from 0 − 210 s. TL glow bands peaked near 634 and 619 K emerge. With increasing grinding time (t), the integrated TL intensity first increases from t = 0 to t = 60 s and then decreases with further increasing grinding time in Figure 5(c,d). The similar applied to other LiTaO$_3$:0.01Tb^{3+},0.005Gd^{3+} in Figure S14 (Supporting Information) and LiTaO$_3$:0.01Tb^{3+},0.015Gd^{3+} in Figure S15 (Supporting Information). It implies that there is a competition between the

ADVANCED
SCIENCE NEWS
www.advancedsciencenews.com
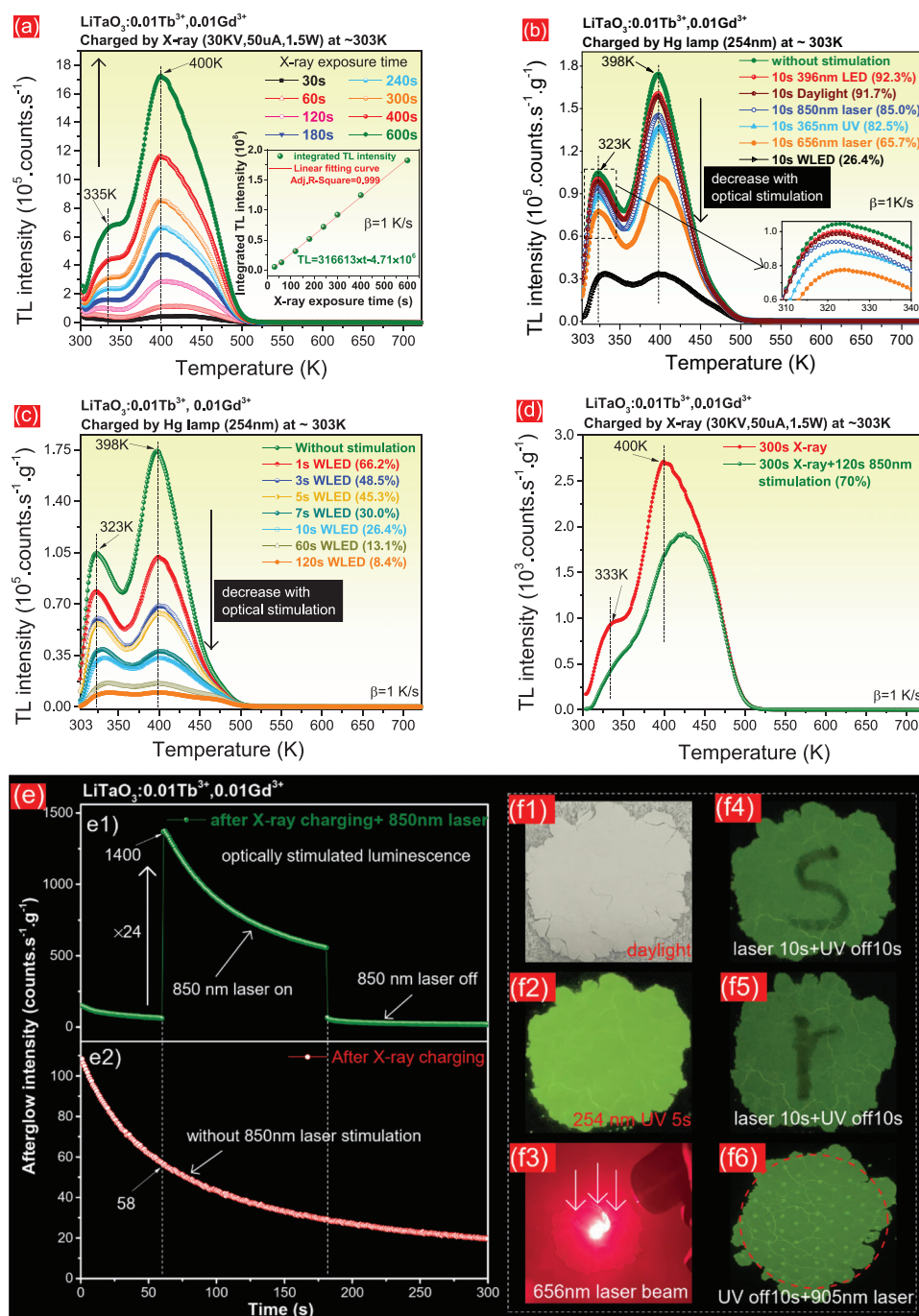
LASER
& PHOTONICS
REVIEWS

www.lpr-journal.org

Figure 4. a) TL glow curves measured at $\beta = 1$ K s^{-1} after exposure to X-rays with different duration from 30 – 600 s, TL glow curves after exposure to 254 nm UV-light charging and then followed by b) different energy photon stimulation for 10 s or by c) a commercial WLED stimulation with different duration from 1 – 300 s, and d) TL fading characteristic after X-ray charging and then followed by delay for 300 s or/and with 850 nm infrared laser stimulation with a duration of 120s for LiTaO$_3$:0.01Tb^{3+},0.01Gd^{3+}. e) RT isothermal decay curve after exposure to X-ray and with 850 nm infrared laser stimulation for 120 s. f1–f6) Rapid write-in and display of "S", "r", and an array of "points" by using the 254 nm UV-light irradiated LiTaO$_3$:0.01Tb^{3+},0.01Gd^{3+} based film with selectively optical stimulation with 656 nm red laser or 905 nm laser array from an iPhone 12Pro.

trapping and de-trapping of the free charge carriers triggered by mechanical grinding stimulation.

Figure 5(e) gives the TL glow curves of LiTaO$_3$:0.01Tb^{3+}, 0.01Gd^{3+} first irradiated by 20 s 254 nm UV-light and then ground in an agate mortar with different duration from 0 – 300 s.

The ratios of the integrated TL intensity irradiated only by 254 nm UV-light illumination to that of with additional different grinding time are listed as percentages in the legend of Figure 5(e). The integrated TL intensity appears to gradually decrease with increasing the grinding time as illustrated in the inset of Figure 5(e). It
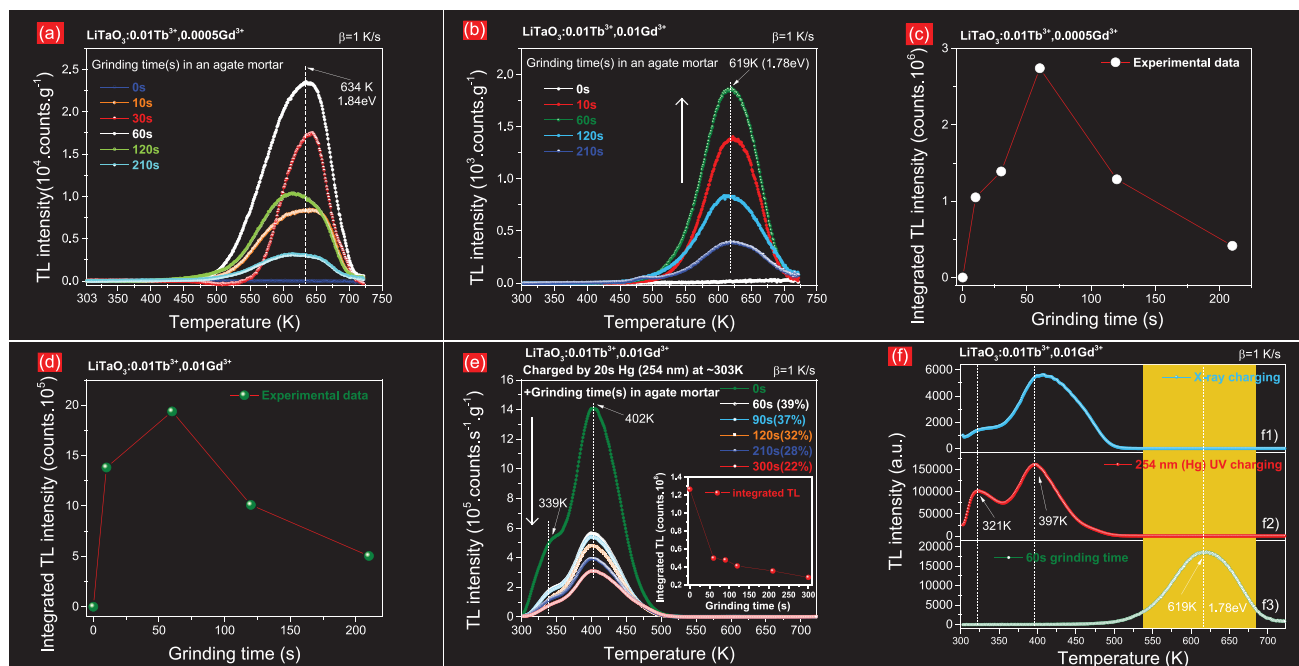
Figure 5. TL glow curves after grinding with different duration in an agate mortar and corresponding integrated TL intensities from 300 – 723 K for a,c) LiTaO$_3$:0.01Tb^{3+},0.005Gd^{3+} and b,d) LiTaO$_3$:0.01Tb^{3+},0.01Gd^{3+}. e) TL glow curves after exposure to 254 nm UV-light charging for 20 s and then followed by grinding with different duration in an agate mortar and f1–f3) A comparison of TL glow curves charged by X-rays, 254 nm UV-light, or 60 s grinding in an agate mortar for LiTaO$_3$:0.01Tb^{3+},0.01Gd^{3+}.

implies that stored charge carriers can be liberated by mechanical stimulation.

Figure 5(f) compares the TL glow curves of LiTaO$_3$:0.01Tb^{3+},0.01Gd^{3+} irradiated by X-rays, 254 nm UV-light, or ground in an agate mortar for 60 s. Compared with that by X-rays or 254 nm UV-light charging in Figure 5(f1,f2), a new TL glow band peaked at ≈619 K is observed in Figure 5(f3) where the phosphor was ground. A similar applied to LiTaO$_3$:0.01Tb^{3+},0.005Gd^{3+} in Figure S13 (Supporting Information). The trap depths for the new TL bands were roughly estimated to be in the range from ≈1.6 to ≈1.8 eV by Equation (1) as denoted in Figure 5, and Figures S14 and S15 (Supporting Information).

2.3. Mechanically Induced Charge Carrier De-Trapping for Continuous Compression Force Sensing and Multimode Anti-Counterfeiting

De-trapping of stored charge carriers in the optimized LiTaO$_3$:0.01Tb^{3+},xGd^{3+} was exploited by mechanical stimulation for continuous compression force sensing application. Since the optimized LiTaO$_3$:0.01Tb^{3+},0.0005Gd^{3+} has the strongest charge carrier storage capacity as shown in Figure 3(i), it was dispersed in an epoxy resin solution to make a hard disc which was then mechanically stimulated with compression force as illustrated in **Figure 6**(a1). Figure 6(a2–a4) illustrates that bright green mechanoluminescence emerges which is visible to the naked eye in the dark when 1000 or 2500 N compression force is utilized. Particularly, persistent mechanoluminescence appears during >7 s in the LiTaO$_3$:0.01Tb^{3+},0.0005Gd^{3+} based hard

disc when 2500 N compression force is continually applied as demonstrated in Figure 6(a2–a8). Commercial ZnS:Cu$^+$,Mn^{2+} phosphor was dispersed in epoxy resin to produce a hard disc for comparison study as shown in Figure 6(b1). Orange mechanoluminescence only emerges in the ZnS:Cu$^+$,Mn^{2+} based disc area where it is touched with the crosshead of the utilized compression machine as shown in Figure 6(b2). Figure 6(b3,b4) shows that the orange mechanoluminescence can only be observed with a duration of ≈2 s although the 2500 N compression force is continually applied with a duration of 120 s.

The optimized LiTaO$_3$:0.01Tb^{3+},0.0005Gd^{3+} and the commercial ZnS:Cu$^+$,Mn^{2+} are dispersed in an epoxy resin solution to fabricate a hard disc as shown in Figure 6(c1). Figure 6(c2–c4) demonstrate that nice compression force distribution sensing can be realized by the green mechanoluminescence from the optimized LiTaO$_3$:0.01Tb^{3+},0.0005Gd^{3+} rather than the commercial ZnS:Cu$^+$,Mn^{2+} when 1000 or 6000 N compression force is applied. Herein, the crosshead moves downward with a distance of ≈2 mm for 6000 N compression force and the shape of the hard disc is slightly changed as demonstrated in Figure 6(c1,c5).

To further again demonstrate the unique feature of the mechanoluminescence from the optimized LiTaO$_3$:0.01Tb^{3+},0.0005Gd^{3+}, the hard disc as utilized in Figure 6(c3,c4) is not re-charged by 254 nm UV-light but is reused as shown in Figure 6(c5). Figure 6(c6–c8) demonstrates that mechanoluminescence mainly comes from the LiTaO$_3$:0.01Tb^{3+},0.0005Gd^{3+} instead of the commercial ZnS:Cu$^+$,Mn^{2+}. Nice compression force sensing can even be realized when the 6000 N compression force is applied again and the crosshead moves downward only with ≈0.2 mm as demonstrated in Figure 6(c6).
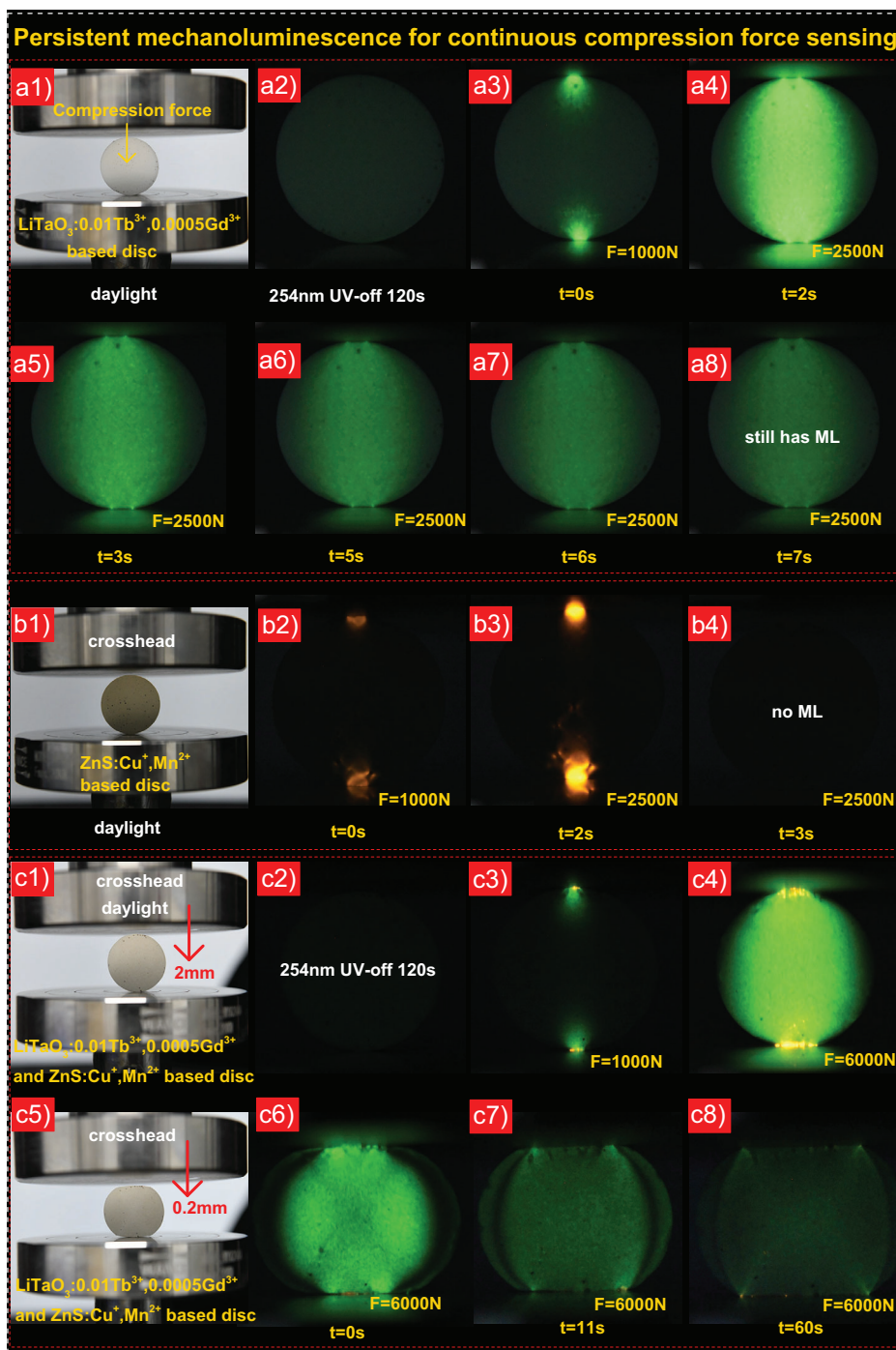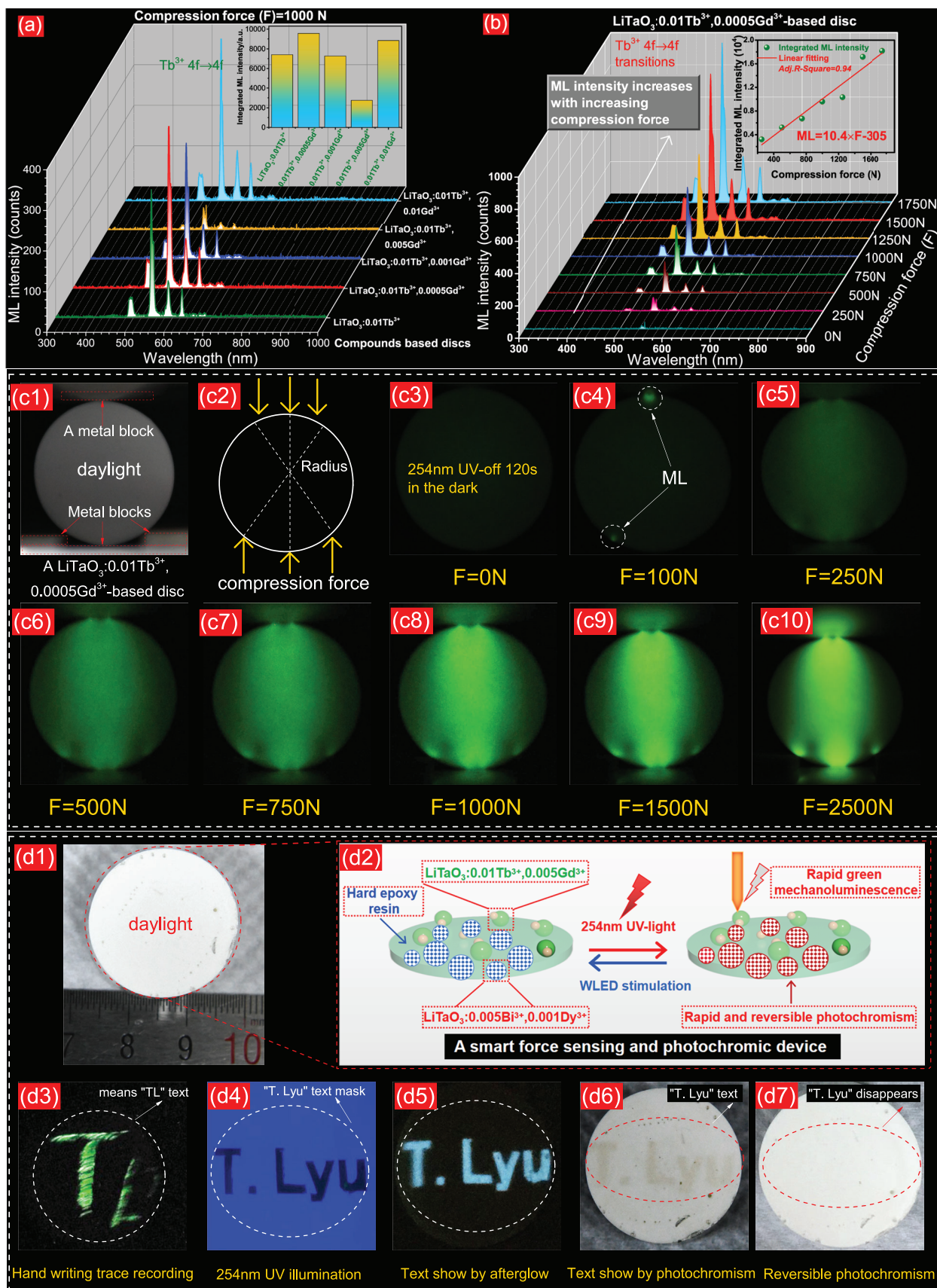
ADVANCED
SCIENCE NEWS
www.advancedsciencenews.com

LASER
& PHOTONICS
REVIEWS

www.lpr-journal.org

Figure 6. a1–a8) Demonstration of persistent mechanoluminescence for continuous compression force sensing by using the optimized LiTaO$_3$:0.01Tb^{3+},0.0005Gd^{3+} based hard epoxy resin disc. Mechanoluminescence properties for b1–b4) commercial ZnS:Cu$^+$,Mn^{2+} based disc and c1–c8) a hard epoxy resin disc containing both optimized LiTaO$_3$:0.01Tb^{3+},0.0005Gd^{3+} and ZnS:Cu$^+$,Mn^{2+}.

Particularly, mechanoluminescence from the LiTaO$_3$:0.01Tb^{3+}, 0.0005Gd^{3+} can be observed for more than 60s when the 6000 N compression force is continually kept as illustrated in Figure 6(c6–c8).

Figure 7(a) compares the mechanoluminescence spectra of the optimized LiTaO$_3$:0.01Tb^{3+}, xGd^{3+}-based hard epoxy resin discs. Characteristic Tb^{3+} ^{5}D$_4 \rightarrow ^7$F$_j$ ($j = 0$–6) line emissions appear when a constant compression force of 1000 N is applied. The integrated mechanoluminescence intensities from 300 to 1000 nm as a function of different compound compositions as utilized in discs are shown as a histogram in the inset of Figure 7(a). The optimized LiTaO$_3$:0.01Tb^{3+},0.0005Gd^{3+} and

ADVANCED
SCIENCE NEWS
www.advancedsciencenews.com

LASER
& PHOTONICS
REVIEWS

www.lpr-journal.org

$LiTaO_3:0.01Tb^{3+},0.01Gd^{3+}$ have the strongest mechanolumines-cence intensities.

Figure 7(b) further gives the mechanoluminescence spectra of the $LiTaO_3:0.01Tb^{3+},0.0005Gd^{3+}$ based hard epoxy resin disc re-peatedly compressed by different compression forces from 0 – 1750 N. The integrated mechanoluminescence intensities from 300 to 900 nm as a function of the used compression force are provided in the inset of Figure 7(b), which can be fitted by a linear formula of ML = $10.4 \times$ F-305. When the mechanoluminescence (ML) intensity is zero, a threshold value of 29 N of the compres-sion force is derived. Figure 7(c1–c10) vividly demonstrates that the $LiTaO_3:0.01Tb^{3+},0.0005Gd^{3+}$ based hard epoxy resin disc can be used as a nice compression force distribution sensing and dis-play sensor when the compression force is gradually applied from 0 – 2500 N in the dark.

To exploit the intense Tb^{3+} $^5D_4 \rightarrow ^7F_j$ (j = 0–6) mechano-luminescence for developing advanced anti-counterfeiting ap-plications, the optimized $LiTaO_3:0.01Tb^{3+},0.0005Gd^{3+}$ storage phosphor is combined with the afterglow and photochromic $LiTaO_3:0.005Bi^{3+},0.001Dy^{3+}$ phosphor to fabricate a smart force sensing and photochromic device as shown in Figure 7(d1). Figure 7(d2) illustrates how multimode luminescence is real-ized by utilizing the developed smart device in which both the $LiTaO_3:0.01Tb^{3+}$, $0.0005Gd^{3+}$ and $LiTaO_3:0.005Bi^{3+},0.001Dy^{3+}$ storage phosphors are uniformly dispersed in epoxy resin. A glass pen is utilized to slightly slide on the surface of the fab-ricated device as shown in Figure 7(d1). Figure 7(d3) shows that a handwriting trace of a "TL" text is visible to the naked eye in the dark because of the mechanically stimulated Tb^{3+} $^5D_4 \rightarrow ^7F_j$ luminescence from $LiTaO_3:0.01Tb^{3+},0.0005Gd^{3+}$. The mechano-luminescence intensity is strong enough to be recorded by a daily used mobile phone to make the ML photograph as shown in Figure 7(d3)

Figure 7(d4) shows that the device is placed underneath a sheet of paper mask and only the phosphors underneath the "T. Lyu" area can be irradiated by 254 nm UV light. Figure 7(d5) shows that bright cyan afterglow "T. Lyu" text ap-pears in the dark, which is because of the persistent Bi^{3+} D-band and Dy^{3+} $4f \rightarrow 4f$ emissions from the 254 nm UV-light irradiated $LiTaO_3:0.005Bi^{3+},0.001Dy^{3+[11c]}$. Note that the after-glow comes from $LiTaO_3:0.005Bi^{3+},0.001Dy^{3+}$ instead of the $LiTaO_3:0.01Tb^{3+},0.0005Gd^{3+}$. Figure 7(d6) shows that brown "T. Lyu" text appears on the surface of the device due to the 254 nm UV-light-induced photochromic phenomenon from the $LiTaO_3:0.005Bi^{3+},0.001Dy^{3+}$. The above results demonstrate that the device with multimode luminescence has potential use in anti-counterfeiting applications.

2.4. X-Ray Induced Charge Carrier Trapping For Conventionally Flat-Panel and Newly Flexible X-Ray Imaging Applications

To explore conventionally flat-panel and newly flexible X-ray imaging applications, the optimized $LiTaO_3:0.01Tb^{3+},0.005Gd^{3+}$

storage phosphor was dispersed in a silicone gel solution to make a bendable film. **Figure 8**(a1) shows that the film was placed underneath a capsule. The capsule is covered by tape and is not transparent. One cannot see the metal spring which is placed inside the capsule during daylight. The film with the capsule was perpendicularly irradiated by X-rays. Figure 8(a2,a3) shows that two flat-panel X-ray imaging photographs of the cap-sule with the spring are visible in the dark because of the ther-mally stimulated Tb^{3+} $^5D_4 \rightarrow ^7F_j$ (j = 0-6) emissions from the $LiTaO_3:0.01Tb^{3+},0.005Gd^{3+}$ in the film kept at room temperature (≈ 298 K) or at ≈ 370 K.

Figure 8(a4) shows that the film was placed underneath a stan-dard lead-based X-ray imaging resolution test plate, which was perpendicularly irradiated by X-rays. Figure 8(a5,a6) shows that a high X-ray imaging spatial resolution of ≈ 20 line pairs mm^{-1} can be obtained, which is higher than that determined by con-ventional scintillator-based screen, like $(C_8H_{20}N)_2Cu_2Br_4$ (9.5 lp mm^{-1}),[28] $CsPbBr_3$ based polymer-ceramic (12.5 lp mm^{-1}),[29] $CH_3NH_3PbI_3$ (6 lp mm^{-1}),[30] and $(C_8H_{20}N)_2MnBr_4$ (5.0 lp mm^{-1}).[31]

Figure 8(b1) shows that a curved electronic board is rolled and connected to a cylinder. The film was then placed under-neath the curved electronic board which was perpendicularly irradiated by X-rays as illustrated in Figure 8(b2). X-rays can pass through both sides of the curved electronic board and the $LiTaO_3:0.01Tb^{3+},0.005Gd^{3+}$ storage phosphor in the film can be charged by formed free charge carriers. Figure 8(b3) shows that an X-ray imaging photograph of the curved electronic board emerges at ≈ 370 K. However, the information on both sides of the curved board overlaps. This implies that there is difficulty in flat-panel X-ray detectors to inspect the structure of curved ob-jects.

Figure 8(c1) shows that the film is very flexible and can be rolled up and then placed underneath the curved electronic board as illustrated in Figure 8(b1). The curved board with the rolled film is irradiated by X-rays as illustrated in Figure 8(c1). After ex-posure to X-rays, the film was rolled out to become a flat film as shown in Figure 8(c2). Figure 8(c3) shows that an X-ray imaging photograph appears in the dark to read out the information of the curved electronic board when the film was kept at ≈ 370 K. This means that the flexible $LiTaO_3:0.01Tb^{3+},0.005Gd^{3+}$ based film has promising use as a smart sensor for X-ray imaging of curved objects.

3. Discussion

3.1. Unraveling Charge Carrier Trapping and De-Trapping Processes in $LiTaO_3:Tb^{3+},Gd^{3+}$ by Various Physical Excitations

The understanding of the trapping, de-trapping, and transport of charge carriers (electrons and holes) is crucial to analyze and even to design luminescent properties of inorganic afterglow and stor-age phosphors[12b, 26a, 33]. The vacuum referred binding (VRBE)

Figure 7. a) Mechanoluminescence (ML) spectra for the optimized $LiTaO_3:0.01Tb^{3+},xGd^{3+}$ dispersed in hard epoxy resin discs when 1000 N compres-sion force is applied. b) ML spectra as a function of compression force from 0 – 1750 N for the optimized $LiTaO_3:0.01Tb^{3+},0.0005Gd^{3+}$ based disc. c1–c10) Illustration on compression force sensing by using a 254 nm UV-light charged $LiTaO_3:0.01Tb^{3+},0.0005Gd^{3+}$ based hard epoxy resin disc. d1–d7) Proof-of-concept multimode anti-counterfeiting applications by combining mechanoluminescence, afterglow, rapid, and reversible photochromism features from a hard epoxy resin disc dispersed with the optimized $LiTaO_3:0.01Tb^{3+}$, $0.0005Gd^{3+}$ and $LiTaO_3:0.005Bi^{3+},0.001Dy^{3+}$ storage phosphors.

ADVANCED
SCIENCE NEWS

www.advancedsciencenews.com

LASER
& PHOTONICS
REVIEWS

www.lpr-journal.org

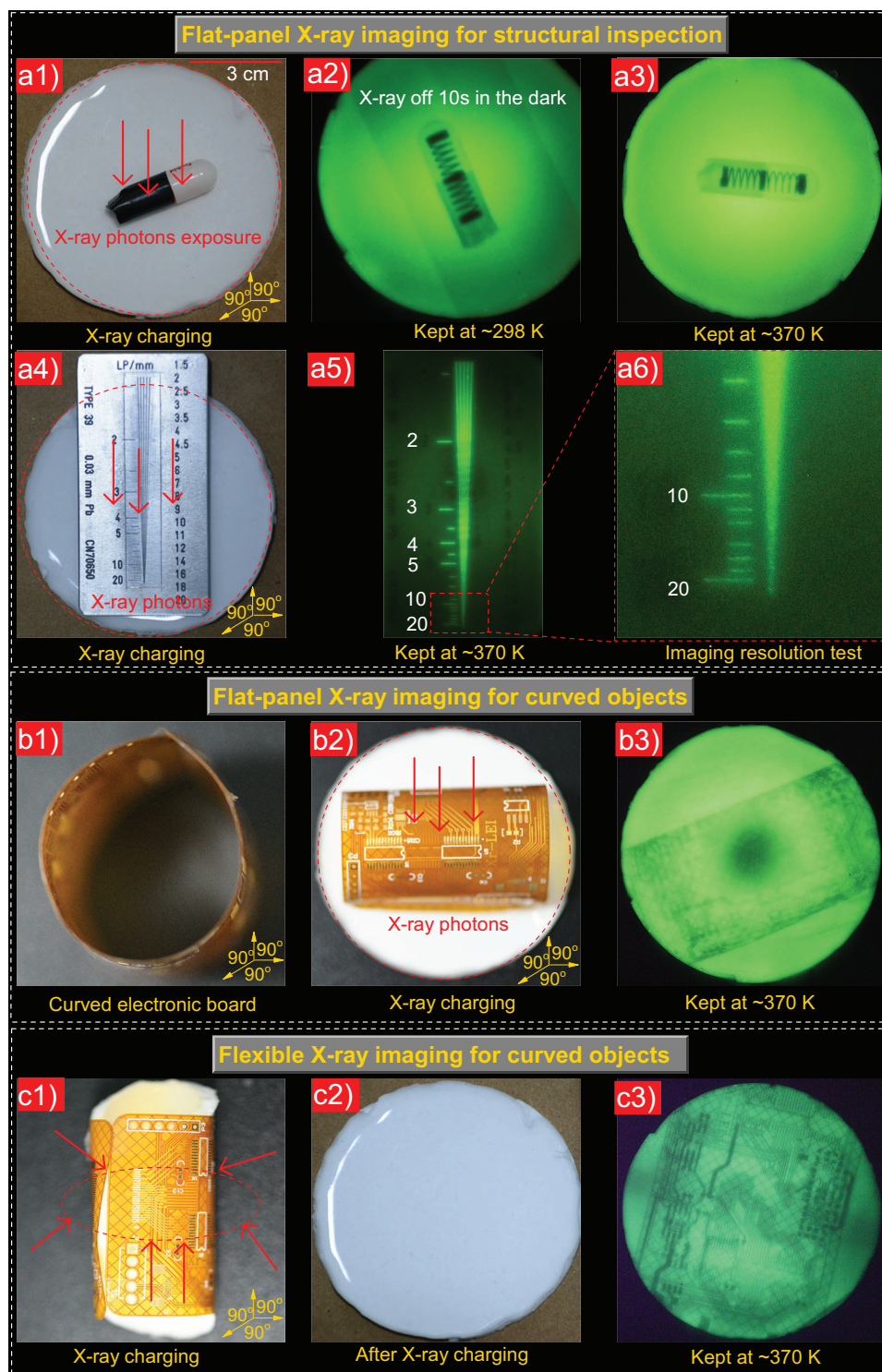**Figure 8.** a1–a3) Proof-of-concept flat-panel X-ray imaging for structural inspection and a4–a6) X-ray imaging resolution test by using a flexible optimized LiTaO$_3$:0.01Tb^{3+},0.005Gd^{3+} based silicon gel film. A comparison of b1–b3) flat-panel X-ray imaging and c1–c3) flexible X-ray imaging for a curved electronic board by using the flexible optimized LiTaO$_3$:0.01Tb^{3+},0.005Gd^{3+} based silicon gel film.

diagram for LiTaO$_3$:Tb^{3+},xGd^{3+} containing the level locations of lanthanides and defect levels are provided in Figure 1(b). The VRBE in the ground states of the divalent and trivalent gadolinium ions are respectively located within the conduction band and the valence band in Figure 1(b). Gd^{3+} then cannot trap an electron and cannot trap a hole, and therefore it cannot act as a recombination center. Yet it might show luminescence usually ≈310 nm by means of energy transfer from the host to Gd^{3+} upon X-ray excitation. However, such Gd^{3+} emission was not observed in Figure 2(f). Possibly the Gd^{3+} emission is quenched by energy transfer from Gd^{3+} to Tb^{3+}.

Figure 3(b) shows that a TL glow band peaked at ≈326 K and a broad TL glow band peaked near ≈408 K in the temperature range from ≈350 to ≈525 K appear in all X-ray irradiated LiTaO$_3$:0.01Tb^{3+},xGd^{3+} (x = 0–0.015) compounds when the typical Tb^{3+} $^5D_4 \rightarrow ^7F_j$ (j = 0–6) emissions are monitored during TL-readout. They are also observed in the optimized LiTaO$_3$:0.01Tb^{3+},xGd^{3+} in Figure 3(i). Figure 3(g) further demonstrates that there is a trap depth distribution from ≈1.0 to ≈1.3 eV. These trap depths are less deep compared with that of the Tb^{3+} hole trap depth (≈1.5 eV) in LiTaO$_3$ as predicted in Figure 1(b). The observed TL bands peaked at ≈326 and ≈408 K are therefore assigned to the liberation of electrons from unintended defects in LiTaO$_3$:Tb^{3+},xGd^{3+}, and recombination with holes trapped at Tb^{4+}. Based on the above-determined trap depths, the VRBE level locations of these unintended defects are ≈−3.6 −4.0 eV, which are collectively named as traps A in Figure 1(b).

During exposure to X-rays, free holes and electrons are produced in the valence band (VB) and the conduction band (CB) of LiTaO$_3$:Tb^{3+},xGd^{3+}. Similar to X-ray-induced activation, free electrons can also be created via the intervalence charge transfer (IVCT) process from the Tb^{3+} ground state to the conduction band (CB) during exposure to 254 nm UV-light which has been experimentally demonstrated in Figure 2(h,i)[22a]. The Tb^{3+}→CB IVCT is illustrated by arrow a in Figure 1(b). The free holes are captured by Tb^{3+}, forming Tb^{4+}[33b,34]. The free electrons are trapped by traps A. With increasing X-ray exposure time, traps A are gradually becoming filled and more produced free charge carriers are available to yield X-ray excited Tb^{3+} $^5D_4 \rightarrow ^7F_j$ emissions as demonstrated in Figures 2(f) and 3(a). Upon thermal activation at RT (≈298 K), the part of the electrons stored at trap A with less deep trapping depth can be gradually liberated to the conduction band. The number of the stored electrons in traps gradually drops, which is evidenced by the decreased TL glow intensities with longer delay time after X-ray charging in LiTaO$_3$:0.01Tb^{3+},0.005Gd^{3+} in Figure 3(f). The released electrons then combine with the holes stored at Tb^{4+}. Energy is released due to the electron-hole recombination, which then excites Tb^{3+} to its excited state. Tb^{3+} persistent luminescence then emerges as illustrated in Figures 2(g) and 3(d,e) because of the Tb^{3+} $^5D_4 \rightarrow ^7F_j$ transitions as denoted in Figure 1(b).

Figure 4(b–d) shows that the TL glow intensity of the 254 nm UV-light irradiated LiTaO$_3$:0.01Tb^{3+},0.01Gd^{3+} drops rapidly with additional photon stimulation. The energy of the used excitation photons changes from 365 nm (≈3.4 eV) to 850 nm (≈1.5 eV), which is larger than the trap depths for traps A as in Figure 1(b). It means that the stimulation energy is high enough to excite the stored electrons from traps A to an excited state level inside the conduction band. The raised electrons will relax to the CB-bottom

and migrate to recombine with the holes trapped at Tb^{4+}, generating Tb^{3+} $^5D_4 \rightarrow ^7F_j$ emissions as shown in Figure 4(e,f) and Figure S12 (Supporting Information).[34]

Like thermal and optical stimulation, the stored electrons at traps A can be liberated by mechanical stimulation. Figure 5(e) shows that the TL glow intensity of 254 nm UV-light irradiated LiTaO$_3$:0.01Tb^{3+},0.01Gd^{3+} gradually drops with increasing the grinding time. The photographs of the LiTaO$_3$:0.01Tb^{3+},0.0005Gd^{3+} based hard epoxy resin disc in Figure 6(a4–a8), (c5−c8) further demonstrate that mechanoluminescence intensity gradually decreases when the compression force is kept at 2500 or 6000 N. The similar applies to LiTaO$_3$:0.01Tb^{3+},0.0005Gd^{3+} based disc as shown in Figure S16 (Supporting Information). The Tb^{3+} $^5D_4 \rightarrow ^7F_j$ mechanoluminescence intensity monotonously drops with increasing the number of cycles of the applied 1000 N compression force. These results collectively imply that the mechanoluminescence in LiTaO$_3$:0.01Tb^{3+},xGd^{3+} is because of the release of the electrons trapped at traps A, possibly by piezoelectricity-triggered activation processes.[17,35]

Figure 5(a,b), and Figure S13–S15 (Supporting Information) show that broad TL glow bands emerge in the temperature range from ≈475 K to 723 K when the LiTaO$_3$:0.01Tb^{3+},xGd^{3+} compounds were ground in an agate mortar. This implies that part of the free electrons produced through mechanical activation has been trapped in new traps created by the grinding. The electron trapping depths are roughly estimated to be from ≈1.6 eV to ≈1.8 eV by using Equation (1) with TL peak maximum (T_m) values and s = 2 × 10^{13} s^{-1}. Based on these depths, the level locations for these traps are from −4.27 eV to −4.51 eV in the VRBE diagram in Figure 1(b), which are collectively denoted as traps B. During mechanical excitation by grinding with agate mortar and pestle, free holes and electrons are formed in the valence band (VB) and the conduction band (CB) of LiTaO$_3$:Tb^{3+},Gd^{3+}, probably by a triboelectricity[36] or piezoelectricity[17a,17b,36c,38] triggered excitation approach. The created holes migrate in the VB and then are captured by Tb^{3+} to form Tb^{4+}. The created electrons freely migrate in the CB, which are then stored at traps B. Note that the electron trapping depths of traps B are deeper than the hole trapping depth of the Tb^{3+} trap. If the hole recombines with the electron there should be some sort of energy transfer back to Tb^{3+}. Figure 5(c,d), Figures S14(b) and S15(b) (Supporting Information) show that the integrated TL intensity first increases and then drops with further increasing grinding time. It means that there is a competitive relation between the force-induced charge carrier storage and the liberation of charge carriers captured at traps B by mechanical excitation.

The role of Tb^{3+} is clear in LiTaO$_3$:0.01Tb^{3+},xGd^{3+}. It creates a stable hole trap and acts as a recombination center with characteristic Tb^{3+} 4f→4f emissions. The role of Gd^{3+} is less clear. It does not participate as a charge carrier trapping and also not as a luminescence center. Yet it does enhance the charge carrier storage capacity performance of LiTaO$_3$:0.01Tb^{3+},xGd^{3+}. Gd^{3+} and Tb^{3+} are 30 pm larger than Ta^{5+}, and most likely will substitute for the ≈ 15 pm smaller Li$^+$ at the 8-fold coordinated site in LiTaO$_3$. There will be a need for charge-compensating defects that speculatively may act as electron traps in the phosphors. One may think of Li$^+$ vacancies to compensate for Gd^{3+} and Tb^{3+}. One may also think of anti-site defects where Li$^+$ occupies the 6-fold

coordinated Ta^{5+} site. Anti-site defects with Li^+ on Ta^{5+} sites and vice versa may also be present in undoped $LiTaO_3$.

3.2. Evaluating Flexible X-Ray Imaging, Multimode Anti-Counterfeiting, Continuous Stress Sensing, and Non-Real-Time Recording Applications

Charge carrier trapping and de-trapping processes have been carefully studied by various physical excitations, which can be exploited for multimode applications. Figure 5(a,b), and Figures S13–S15 (Supporting Information) demonstrate that charge carrier storage with TL glow peaked at ≈564-634 K appears in mechanically stimulated $LiTaO_3$:$0.01Tb^{3+}$,xGd^{3+}. Since the TL peaks are well above room temperature (≈298 K), charge carriers can be stably stored at RT. It means that $LiTaO_3$:$0.01Tb^{3+}$,xGd^{3+} has potential use in non-real-time force recording applications.[19] Multimode luminescence is also realized in $LiTaO_3$:$0.01Tb^{3+}$,xGd^{3+}, i.e., X-ray excited Tb^{3+} emission (Figure 2(f)), afterglow (Figure 3(d,e), optically stimulated luminescence by wide range photon stimulation (Figure 4), and bright mechanoluminescence (Figure 10). Together with rapid and reversible photochromic features in $LiTaO_3$:$0.005Bi^{3+}$,$0.001Dy^{3+}$, $LiTaO_3$:$0.01Tb^{3+}$,xGd^{3+} storage phosphors with various luminescence then have promising utilization in multimode anti-counterfeiting applications, for example in Figures 4 and 7(d), and Figure S17 (Supporting Information). The optimized $LiTaO_3$:$0.01Tb^{3+}$,xGd^{3+} compounds have excellent charge carrier storage capacity (Figure 3(i)), and charge carriers can be linearly stored as a function of X-ray exposure time (Figure 4(a)) in $LiTaO_3$:$0.01Tb^{3+}$,xGd^{3+}. It suggests that the optimized $LiTaO_3$:$0.01Tb^{3+}$,xGd^{3+} dosimeters have potential use in both the conventional flat-panel and newly flexible X-ray imaging applications as illustrated in Figure 8.

Figure 6(b1–b4) demonstrates that mechanoluminescence only appears in a small part of the ZnS:Cu^+,Mn^{2+} based hard epoxy resin where it touches with the crosshead of the compression machine. It implies that the ZnS:Cu^+,Mn^{2+} based disc is not suitable for compression force distribution sensing. The mechanoluminescence emerges only for a short duration of ≈2 s although the 2500 N compression force is continually kept. Possibly the mechanoluminescence observed in ZnS:Cu^+,Mn^{2+} based disc is mainly induced by a triboelectricity-triggered excitation process[37a,39]. Commercial ZnS:Cu^+,Mn^{2+} phosphor has been heated to 723 K or ground in an agate mortar with a pestle. However, no obvious TL signal was observed from 300 to 723 K. It means that no charge carriers are stored at RT. ZnS:Cu^+,Mn^{2+} has a small band gap (≈3.5 eV). Possibly shallow traps exist in ZnS:Cu^+,Mn^{2+}, but the charge carriers captured in the shallow traps may have already faded at RT. Unlike ZnS:Cu^+,Mn^{2+}, intense green Tb^{3+} $^5D_4 \to {}^7F_j$ mechanoluminescence appears homogeneously in the $LiTaO_3$:$0.01Tb^{3+}$,$0.0005Gd^{3+}$ based hard epoxy resin disc in Figure 6(a) when 2500 N compression force is applied. Particularly, the mechanoluminescence from $LiTaO_3$:$0.01Tb^{3+}$,$0.0005Gd^{3+}$ based disc can be observed >60 s in Figure 6(c) when 6000 N compression force is continually kept. It indicates that the green mechanoluminescence comes from the de-trapping of charge carriers stored at traps A as evidenced in Figures 3(b) and 5(e), and Figure S16 (Supporting

Information), probably by a piezoelectricity-triggered excitation route[5c,40]. The ML intensity linearly depends on the intensity and how the compression force is applied in the disc as evidenced in Figure 7(b,c). These results suggest that $LiTaO_3$:$0.01Tb^{3+}$,xGd^{3+} storage phosphors with excellent charge carrier storage capacity have promising use in continuous compression stress sensing.

4. Conclusions

In this work, a high-performance and versatile energy storage $LiTaO_3$:$0.01Tb^{3+}$,xGd^{3+} perovskite was discovered. The trapping and release processes of charge carriers in $LiTaO_3$:$0.01Tb^{3+}$,xGd^{3+} have been carefully studied and well explained by combining the vacuum-referred binding diagram establishment, spectroscopy, thermoluminescence, and mechanoluminescence. A TL glow band peaked at ≈326 K and broad TL bands peaked at ≈408–432 K in the temperature range from 350 to 525 K appear in the X-ray irradiated $LiTaO_3$:$0.01Tb^{3+}$,xGd^{3+} at β = 1 K s^{-1}. They are assigned to electron-trapping defects. During TL-readout, the electrons stored are released by thermal activation to recombine with the holes trapped at Tb^{4+}, producing typical Tb^{3+} $^5D_4 \to {}^7F_j$ (j = 0–6) emissions. More than 40 h Tb^{3+} afterglow is visible in the X-ray irradiated $LiTaO_3$:$0.01Tb^{3+}$,$0.005Gd^{3+}$. The optimized $LiTaO_3$:$0.01Tb^{3+}$,xGd^{3+} (x = 0.0005–0.01) have very excellent charge carrier storage capacity. Particularly, the ratios of the integrated TL intensity of the optimized $LiTaO_3$:$0.01Tb^{3+}$,$0.005Gd^{3+}$ charged by X-rays to that of the commercial $BaFBr(I)$:Eu^{2+}, Al_2O_3:C chip, or $SrAl_2O_4$:Eu^{2+},Dy^{3+} are respectively 7.2, 12.2, and 7.4 which are excellent values so far. Charge carriers can be stably stored in the $LiTaO_3$:$0.01Tb^{3+}$,$0.005Gd^{3+}$ with a duration of >1200 h. Like thermal stimulation, the stored charge carriers in $LiTaO_3$:$0.01Tb^{3+}$, xGd^{3+} can be efficiently liberated to generate Tb^{3+} $^5D_4 \to {}^7F_j$ emissions by mechanical excitation or wide range 365 nm UV-light to 850 nm infrared light stimulation. Similar to X-ray and $Tb^{3+} \to CB$ IVCT excitations, the generation and storage of charge carriers by mechanical excitation appears in $LiTaO_3$:$0.01Tb^{3+}$,xGd^{3+}. $LiTaO_3$:$0.01Tb^{3+}$,xGd^{3+} combines the features of X-ray excited luminescence, afterglow, optically stimulated luminescence, persistent mechanoluminescence, and force-induced charge carrier storage. It well responds to various stimuli channels, i.e., wide-range X-rays to 850 nm infrared photons, thermal activation, mechanical force grinding, or compression. A combination of these features in the $LiTaO_3$:$0.01Tb^{3+}$,xGd^{3+} with rapid and reversible photochromic features in $LiTaO_3$:$0.005Bi^{3+}$, $0.001Dy^{3+}$ enables promising multimode anti-counterfeiting, flexible X-ray imaging, continuous compression force sensing, and non-real-time recording applications. This work not only reports novel $LiTaO_3$:$0.01Tb^{3+}$,xGd^{3+} with excellent charge carrier storage capacity, but also deepens our understanding of multimode luminescence and how charge carriers can be trapped and de-trapped by various physical excitations with X-rays, wide range deep UV (254 nm) to 850 nm infrared light, mechanical grinding, and compression force. This work can trigger more scientists to exploit the development of advanced storage phosphors for multimode luminescence applications.

5. Experimental Section

Li_2CO_3 (99.99%) chemical was purchased from Shanghai Makclin Biochemical Company. The other starting chemicals were bought from Shanghai Aladdin Biochemical Technology company and stored in a dry room. The $LiTaO_3$:$0.01Tb^{3+}$,xGd^{3+} ($x = 0 - 0.015$) storage phosphors were prepared by utilizing a typical high-temperature solid-state reaction technique. About 1.30 g of appropriate stoichiometric mixture of Li_2CO_3 (99.99%), Ta_2O_5 (99.99%), Tb_4O_7 (99.99%), and Gd_2O_3 (99.99%) was homogeneously mixed in an agate mortar with the help of a pestle and acetone solution for ≈ 20 min. The mixed mixture was placed in a covered corundum crucible and then heated at 1200 °C with a duration of 360 min in a tube furnace under an ambient atmosphere. The utilized heating rate for the tube furnace is 3 °C min^{-1}. After that, the synthesized compounds were naturally cooled to room temperature (RT, $\approx$298 K). The obtained compounds were ground again prior to further measurements. To optimize the charge carrier storage capacity, the optimized $LiTaO_3$:$0.01Tb^{3+}$,xGd^{3+} ($x = 0 - 0.015$) compounds were heated at 1250 °C with a duration of 400 min. The photochromic $LiTaO_3$:$0.005Bi^{3+}$,$0.001Dy^{3+}$ storage phosphor for anti-counterfeiting application was synthesized by using a method as given.[11c]

To study mechanoluminescence properties of the synthesized $LiTaO_3$:$0.01Tb^{3+}$,xGd^{3+} ($x = 0 - 0.015$) compounds, ≈ 0.82 g phosphor powder was dispersed in ≈ 6.56 g epoxy resin to make a hard disc which has a diameter of 2.5 cm and a thickness of ≈ 0.65 cm. The mixture was placed in a silicon gel-based mold and then heated at 80 °C for 2.5 h in a vacuum. After that, the mixture was naturally cooled to RT and a hard disc was obtained. Commercial ZnS:Cu$^+$,Mn^{2+} phosphor was bought from Shanghai Keyan Phosphor Technology Co., Ltd (https://kpt.net.cn/en/). To study flat-panel and flexible X-ray imaging applications, ≈ 0.70 g optimized $LiTaO_3$:$0.01Tb^{3+}$,$0.005Gd^{3+}$ storage phosphor was first sieved by a 200 mesh screen and then dispersed in ≈ 4.20 g silicone gel (Sylgard 184, Dow Corning) to produce a flexible film on a polished sapphire mold with a diameter of ≈ 6 cm. The mold filled with the mixture was heated at 70 °C for 2.5 h in a vacuum. Photographs shown in this manuscript were taken using a commercial Nikon D850 camera or an iPhone 12Pro.

X-ray diffraction patterns, transmission electron microscope images, and reflectivity spectra for the made $LiTaO_3$:$0.01Tb^{3+}$,xGd^{3+} ($x = 0 - 0.015$) compounds were measured by a Rigaku SmartLa X-ray diffraction facility, an FEI/ Talos F200X G2 setup, and a Shimadzu UV-2550 spectrophotometer. Photoluminescence emission (PL) and excitation spectra (PLE) in the spectral range from 125–360 nm were collected at 10 K with a special VUV spectroscopy station BSRF (Beijing Synchrotron Radiation Facility). Above 200 nm PLE, PL spectra, and RT (298 K) isothermal decay spectra were collected by an Edinburgh FLS920 fluorescence spectrometer. All the recorded emission spectra were corrected by the quantum efficiencies of the used photomultiplier at different wavelengths. All the PLE spectra were corrected by the intensities of the utilized Xenon lamp at different wavelengths. X-ray excited emission intensities as a function of X-ray exposure time, 254 nm UV-light or X-ray charged thermoluminescence (TL) curves, room temperature isothermal decay curves, and optically stimulated luminescence were collected by a facility. It combined a thermostat, a Japan Hamamatsu photomultiplier (PMT, type R928P), a shutter, a commercial Hg lamp, a MOXTEK TUB00083-2 X-ray tube, a BG-39 filter, and different optical excitation sources like a commercial WLED (58 mW cm^{-2}) and a 656 nm red laser beam (8.4 mW cm^{-2}) for optically stimulated luminescence measurements. For a fair TL intensity comparison, the sample had a constant mass of $\approx$0.0300 g, which was then uniformly placed on a metal circle sample holder with a diameter of $\approx$0.8 cm. The X-ray intensity was fixed by operating the MOXTEK TUB00083-2 X-ray tube at 30 KV, 50 μA, and 1.5 W. The dose rate of the X-rays applied to the studied samples is ≈ 0.5 Gy min^{-1}. The 254 nm UV light with a light density of ≈ 300 μW cm^{-2} was fixed from a 4 W Hg lamp. The TL intensities were corrected by the sample mass and the X-ray or 254 nm UV-light irradiation time. Since the TL intensities were measured in the same TL setup with a fixed configuration, they were comparable. Prior to measurements, samples were kept at 450 °C for 120 s to empty stored electrons and holes in traps. The commercial BaFBr(I):Eu^{2+} X-ray storage phosphor and Al_2O_3:C chip were purchased from the Agfa-Gevaert and LANDAUER companies, respectively.

Supporting Information

Supporting Information is available from the Wiley Online Library or from the author.

Conflict of Interest

The authors declare no conflict of interest

Data Availability Statement

The data that support the findings of this study are available on request from the corresponding author. The data are not publicly available due to privacy or ethical restrictions

Keywords

[1] R. Arppe, T. J. Sørensen, *Nat. Rev. Chem.* **2017**, *1*, 0031.
[2] a) W. Ren, G. Lin, C. Clarke, J. Zhou, D. Jin, *Adv. Mater.* **2019**, *32*, 1901430; b) X. Zhou, L. Ning, J. Qiao, Y. Zhao, P. Xiong, Z. Xia, *Nat. Commun.* **2022**, *13*, 7589.
[3] Z. Hu, X. Huang, Z. Yang, J. Qiu, Z. Song, J. Zhang, G. Dong, *Light: Sci. Appl.* **2021**, *10*, 140.
[4] J. Tan, Q. Li, S. Meng, Y. Li, J. Yang, Y. Ye, Z. Tang, S. Qu, X. Ren, *Adv. Mater.* **2021**, *33*, 2006781.
[5] a) Y. Zhao, D. Peng, G. Bai, Y. Huang, S. Xu, J. Hao, *Adv. Funct. Mater.* **2021**, *31*, 2010265; b) Y. Du, Y. Jiang, T. Sun, J. Zhao, B. Huang, D. Peng, F. Wang, *Adv. Mater.* **2019**, *31*, 1807062; c) C. Wu, S. Zeng, Z. Wang, F. Wang, H. Zhou, J. Zhang, Z. Ci, L. Sun, *Adv. Funct. Mater.* **2018**, *28*, 1803168.
[6] X. Huang, Q. Guo, D. Yang, X. Xiao, X. Liu, Z. Xia, F. Fan, J. Qiu, G. Dong, *Nat. Photonics* **2020**, *14*, 82.

[7] C. Mongin, P. Moroz, M. Zamkov, F. N. Castellano, *Nat. Chem.* **2018**, *10*, 225.

[8] a) B. Zhou, L. Yan, J. Huang, X. Liu, L. Tao, Q. Zhang, *Nat. Photonics* **2020**, *14*, 760; b) P. Pei, R. Wei, B. Wang, J. Su, Z. Zhang, W. Liu, *Adv. Funct. Mater.* **2021**, *31*, 2102479.

[9] Z. Zeng, B. Huang, X. Wang, L. Lu, Q. Lu, M. Sun, T. Wu, T. Ma, J. Xu, Y. Xu, S. Wang, Y. Du, C.-H. Yan, *Adv. Mater.* **2020**, *32*, 2004506.

[10] a) Z. Song, Y. Shang, Q. Lou, J. Zhu, J. Hu, W. Xu, C. Li, X. Chen, K. Liu, C.-X. Shan, X. Bai, *Adv. Mater.* **2022**, *35*, 2207970; b) K. Jiang, L. Zhang, J. Lu, C. Xu, C. Cai, H. Lin, *Angew. Chem., Int. Ed.* **2016**, *55*, 7231.

[11] a) P. Huang, Z. Wen, Y. Yu, J. Xiao, Z. Wei, T. Lyu, *Mater. Chem. Front.* **2023**, *7*, 168; b) T. Lyu, P. Dorenbos, P. Xiong, Z. Wei, *Adv. Funct. Mater.* **2022**, *32*, 2206024; c) T. Lyu, P. Dorenbos, C. Li, Z. Wei, *Laser Photonics Rev.* **2022**, *16*, 2200055; d) T. Lyu, P. Dorenbos, C. Li, S. Li, J. Xu, Z. Wei, *Chem. Eng. J.* **2022**, *435*, 135038.

[12] a) T. Lyu, P. Dorenbos, *Laser Photonics Rev.* **2022**, *16*, 2200304; b) T. Lyu, P. Dorenbos, *Chem. Eng. J.* **2020**, *400*, 124776; c) T. Lyu, P. Dorenbos, *J. Mater. Chem. C* **2018**, *6*, 369; d) T. Lyu, P. Dorenbos, *J. Mater. Chem. C* **2018**, *6*, 6240.

[13] T. Lyu, P. Dorenbos, *Chem. Eng. J.* **2019**, *372*, 978.

[14] T. Lyu, Doctoral Thesis Doctoral Thesis, Delft University of Technology, Delft, **2020-09-09**, 2020.

[15] a) J. Ning, Y. Zheng, Y. Ren, L. Li, X. Shi, D. Peng, Y. Yang, *Sci. Bull.* **2022**, *67*, 707; b) X. Zhang, D. Yang, S. Wu, X. Xu, R. Ma, D. Peng, Z. Wang, S. Wang, *Dalton Trans.* **2022**, *51*, 10457; c) D. Peng, Y. Jiang, B. Huang, Y. Du, J. Zhao, X. Zhang, R. Ma, S. Golovynskyi, B. Chen, F. Wang, *Adv. Mater.* **2020**, *32*, 1907747; d) X. Li, C. Wang, Y. Zheng, Z. Huang, J. Luo, M. Zhu, T. Liang, B. Ren, X. Zhang, D. Wang, Z. Ren, S. Qu, W. Zheng, X. Wei, D. Peng, *Mater. Des.* **2023**, *225*, 111589.

[16] a) D. Peng, C. Wang, R. Ma, S. Mao, S. Qu, Z. Ren, S. Golovynskyi, C. Pan, *Sci. Bull.* **2021**, *66*, 206; b) C. Wang, D. Peng, C. Pan, *Sci. Bull.* **2020**, *65*, 1147.

[17] a) S. Liu, Y. Zheng, D. Peng, J. Zhao, Z. Song, Q. Liu, *Adv. Funct. Mater.* **2023**, *33*, 2209275; b) S. Zhou, Y. Cheng, J. Xu, H. Lin, Y. Wang, *Adv. Funct. Mater.* **2022**, *32*, 2208919; c) J. Yin, X. Huo, X. Cao, R. Li, Y. Zhou, T. Jiang, L. Wang, Z. Wu, Z. L. Wang, *ACS Mater. Lett.* **2023**, *5*, 11.

[18] a) Z. Huang, B. Chen, B. Ren, D. Tu, Z. Wang, C. Wang, Y. Zheng, X. Li, D. Wang, Z. Ren, S. Qu, Z. Chen, C. Xu, Y. Fu, D. Peng, *Adv. Sci.* **2023**, *10*, 2204925; b) T. Hu, T. Gao, B. Wang, T. Yu, D. Wen, Y. Cheng, Q. Zeng, *J. Mater. Chem. C* **2022**, *10*, 9554.

[19] Y. Xiao, P. Xiong, S. Zhang, K. Chen, S. Tian, Y. Sun, P. Shao, K. Qin, M. G. Brik, S. Ye, D. Chen, Z. Yang, *Chem. Eng. J.* **2023**, *453*, 139671.

[20] Y. Zhuang, D. Tu, C. Chen, L. Wang, H. Zhang, H. Xue, C. Yuan, G. Chen, C. Pan, L. Dai, R.-J. Xie, *Light: Sci. Appl.* **2020**, *9*, 182.

[21] T. Lyu, P. Dorenbos, Z. Wei, *Chem. Eng. J.* **2023**, *461*, 141685.

[22] a) T. Lyu, P. Dorenbos, *Chem. Mater.* **2020**, *32*, 1192; b) P. Dorenbos, *J. Mater. Chem. C* **2023**; c) P. Dorenbos, *Opt. Mater.* **2019**, *91*, 333; d) P. Dorenbos, *Opt. Mater.* **2017**, *69*, 8.

[23] Y. Yang, B. Lou, Y. Ou, F. Su, C.-G. Ma, C.-K. Duan, P. Dorenbos, H. Liang, *Inorg. Chem.* **2022**, *61*, 7654.

[24] a) C. Liu, Z. Qi, C.-G. Ma, P. Dorenbos, D. Hou, S. Zhang, X. Kuang, J. Zhang, H. Liang, *Chem. Mater.* **2014**, *26*, 3709; b) R. Zhou, F. Ma, F. Su, Y. Ou, Z. Qi, J. Zhang, Y. Huang, P. Dorenbos, H. Liang, *Inorg. Chem.* **2020**, *59*, 17421.

[25] M. Nikl, R. Morlotti, C. Magro, R. Bracco, *J. Appl. Phys.* **1996**, *79*, 2853.

[26] a) H. Luo, A. J. J. Bos, P. Dorenbos, *J. Phys. Chem. C* **2017**, *121*, 8760; b) W. Hoogenstraaten, *Philips Res. Rep* **1958**, *13*, 515; c) A. J. J. Bos, *Radiat. Meas.* **2006**, *41*, S45; d) J. Ueda, S. Miyano, S. Tanabe, *ACS Appl. Mater. Interfaces* **2018**, *10*, 20652.

[27] J. Mendes-Filho, V. Lemos, F. Cerdelra, *J. Raman Spectrosc.* **1984**, *15*, 367.

[28] X. Ou, X. Qin, B. Huang, J. Zan, Q. Wu, Z. Hong, L. Xie, H. Bian, Z. Yi, X. Chen, Y. Wu, X. Song, J. Li, Q. Chen, H. Yang, X. Liu, *Nature* **2021**, *590*, 410.

[29] B. Su, J. Jin, K. Han, Z. Xia, *Adv. Funct. Mater.* **2022**, *33*, 2210735.

[30] W. Chen, M. Zhou, Y. Liu, X. Yu, C. Pi, Z. Yang, H. Zhang, Z. Liu, T. Wang, J. Qiu, S. F. Yu, Y. Yang, X. Xu, *Adv. Funct. Mater.* **2022**, *32*, 2107424.

[31] S. Deumel, A. van Breemen, G. Gelinck, B. Peeters, J. Maas, R. Verbeek, S. Shanmugam, H. Akkerman, E. Meulenkamp, J. E. Huerdler, M. Acharya, M. García-Batlle, O. Almora, A. Guerrero, G. Garcia-Belmonte, W. Heiss, O. Schmidt, S. F. Tedde, *Nat. Electron.* **2021**, *4*, 681.

[32] T. Jiang, W. Ma, H. Zhang, Y. Tian, G. Lin, W. Xiao, X. Yu, J. Qiu, X. Xu, Y. Yang, D. Ju, *Adv. Funct. Mater.* **2021**, *31*, 2009973.

[33] a) H. Luo, P. Dorenbos, *J. Mater. Chem. C* **2018**, *6*, 4977; b) H. Luo, A. J. J. Bos, P. Dorenbos, *J. Phys. Chem. C* **2016**, *120*, 5916; c) Q. Du, J. Ueda, R. Zheng, S. Tanabe, *Adv. Opt. Mater.* **2023**, *11*, 2202612; d) J. Ueda, J. Xu, S. Takemura, T. Nakanishi, S. Miyano, H. Segawa, S. Tanabe, *ECS J. Solid State Sci. Technol.* **2021**, *10*, 116003; e) J. Ueda, *Bull. Chem. Soc. Jpn.* **2021**, *94*, 2807.

[34] a) J. Ueda, S. Miyano, J. Xu, P. Dorenbos, S. Tanabe, *Adv Photonics Res* **2021**, *2*, 2000102; b) J. Xu, S. Tanabe, *J. Lumin.* **2019**, *205*, 581; c) N. Majewska, T. Lesniewski, S. Mahlik, M. Grinberg, D. Kulesza, J. Ueda, E. Zych, *J. Phys. Chem. C* **2020**, *124*, 20340; d) D. Kulesza, A. J. J. Bos, E. Zych, *Acta Mater.* **2022**, *231*, 117852.

[35] a) A. Dobrowolska, A. J. J. Bos, P. Dorenbos, *J. Lumin.* **2016**, *170*, 497; b) Z. Liu, L. Zhao, X. Yang, L. Yang, H. Zhang, W. Zeng, X. Yu, J. Qiu, X. Xu, *Chem. Eng. J.* **2020**, *401*, 126119.

[36] a) C.-N. Xu, T. Watanabe, M. Akiyama, X.-G. Zheng, *Appl. Phys. Lett.* **1999**, *74*, 2414; b) D. Tu, C.-N. Xu, A. Yoshida, M. Fujihala, J. Hirotsu, X.-G. Zheng, *Adv. Mater.* **2017**, *29*, 1606914; c) J.-C. Zhang, X. Wang, G. Marriott, C.-N. Xu, *Prog. Mater. Sci.* **2019**, *103*, 678; d) D. Tu, C.-N. Xu, S. Kamimura, Y. Horibe, H. Oshiro, L. Zhang, Y. Ishii, K. Hyodo, G. Marriott, N. Ueno, X.-G. Zheng, *Adv. Mater.* **2020**, *32*, 1908083.

[37] a) Y. Bai, F. Wang, L. Zhang, D. Wang, Y. Liang, S. Yang, Z. Wang, *Nano Energy* **2022**, *96*, 107075; b) Y. Bai, X. Guo, B. Tian, Y. Liang, D. Peng, Z. Wang, *Adv. Sci.* **2022**, *9*, 2203249; c) Z. Ma, Y. Han, Y. Bai, B. Liu, Z. Wang, *Chem. Eng. J.* **2023**, *456*, 141122.

[38] a) B. Tian, Z. Wang, A. T. Smith, Y. Bai, J. Li, N. Zhang, Z. Xue, L. Sun, *Nano Energy* **2021**, *83*, 105860; b) C. Chen, Y. Zhuang, X. Li, F. Lin, D. Peng, D. Tu, A. Xie, R.-J. Xie, *Adv. Funct. Mater.* **2021**, *31*, 2101567; c) B. P. Chandra, K. K. Shrivastava, *J. Phys. Chem. Solids* **1978**, *39*, 939.

[39] Z. Ma, J. Zhou, J. Zhang, S. Zeng, H. Zhou, A. T. Smith, W. Wang, L. Sun, Z. Wang, *Mater. Horiz.* **2019**, *6*, 2003.

[40] a) P. Jha, B. P. Chandra, *Luminescence* **2014**, *29*, 977; b) J.-C. Zhang, Y.-Z. Long, X. Yan, X. Wang, F. Wang, *Chem. Mater.* **2016**, *28*, 4052; c) A. Feng, P. F. Smet, *Materials* **2018**, *11*, 484; d) J. Hao, C.-N. Xu, *MRS Bull.* **2018**, *43*, 965.